Water Resources Research®

RESEARCH ARTICLE

Key Points:

- Under open-surface condition, our data supports for the existence of the logarithmic layer near the river bed. Under ice-covered condition, it is challenging to identify the existence of the logarithmic layers
- The ice cover alters the secondary flow pattern, and relocates the position of the main circulation
- Under ice-covered condition, shear stresses are elevated near banks even at relatively low discharge

Correspondence to:

T. B. Le,
trung.le@ndsu.edu

On the Impacts of Ice Cover on Flow Profiles in a Bend

Berkay Koyuncu[1] and Trung Bao Le[1,2] (ORCID)

[1]Environmental and Conservation Sciences, College of Engineering, North Dakota State University, Fargo, ND, USA, [2]Department of Civil, Construction and Environmental Engineering, North Dakota State University, Fargo, ND, USA

Abstract We investigate the impact of ice coverage on flow and bed shear stress profiles in a river bend. We perform field measurements using Acoustic Doppler Current Profiler in a bend of the Red River, North Dakota, the United States. Field campaigns were carried out under both open-surface and ice-covered conditions in 2020 and 2021. Our results show that the time-averaged velocity profile follows closely the quartic solution (Guo et al., 2017, under full ice coverage. While the flow profile under open-surface condition follows closely the logarithmic law near the bed, it is challenging to identify the logarithmic layers in our measured data under ice-covered condition. Our results also show that the impact of ice coverage is most significant near both banks where the vertical velocity profile is modified significantly due to the interaction of turbulent flows with the ice cover. Our results suggest that the bend curvature and ice coverage both have significant impacts on the velocity profile as well as the distribution of the bed shear stresses. Our findings provide new insights on sediment transport processes of ice-covered rivers, especially during the break-up period when the surface coverage changes rapidly.

Plain Language Summary As climate change continues, shorter winter is expected to result in a less number of ice-covered days for natural streams. While ice cover has been linked to a variety of eco-hydraulic issues, it is unclear on the relationship between ice coverage and changes in river hydrodynamics. Thus the understanding of ice-covered flows has become a critical issue to predict morphological and ecological conditions of river flows in cold regions. This study aims to identify the impact of ice by conducting field-scale observations and comparing with analytical models. Our results show that the ice layer alters flow patterns beneath it, which leads to active areas near banks. This new finding suggests that ice cover might play a significant role in sediment transport near banks in Spring when its extension can change sharply in a short amount of time.

1. Introduction

Ice coverage has been recognized as an important hydraulic aspect of alluvial channels for a long time (Guo et al., 2017). The role of river ice in ecological (Prowse, 2001b), morphological (Ettema, 2002), and hydraulic aspects (Prowse, 2001a) have been well recognized. Recent evidence suggests that it plays an important role in regulating large-scale turbulent structures (Biron et al., 2019) and ultimately channel lateral migration (Turcotte et al., 2011). Under the impact of climate change, the loss of river ice (Yang et al., 2020) is expected to lead to detrimental consequences for aquatic environments (Thellman et al., 2021). Despite its importance, our understanding of icy flows is rather limited because of challenges related to field measurements. The goal of this study is to examine the impacts of ice coverage on flow profiles in a meandering bend, a common feature of the riverine system.

Field measurement of turbulent flows in rivers is challenging even under open-surface condition (Petrie et al., 2013), especially when secondary flow is observed (Moradi et al., 2019). The measurement under ice coverage poses a different set of safety and accuracy issues when instruments are placed beneath the ice layer (Biron et al., 2019). Under a fully frozen surface, it is necessary to drill holes across the ice layer in order to make the sensor submerged. In particular, it is challenging to obtain reliable data close to the ice layer as well as the river bed (Attar & Li, 2013).

As the top surface is frozen during winter (Ettema, 2002), it provides an additional layer of roughness in addition to the river bed. The presence of the ice coverage alters the spatial distribution of the entire velocity profile. Ice coverage creates a significant difference between the physical characteristics of surface and bed, forming an asymmetrical flow configuration (Chen et al., 2018; Parthasarathy & Muste, 1994). The asymmetrical flow
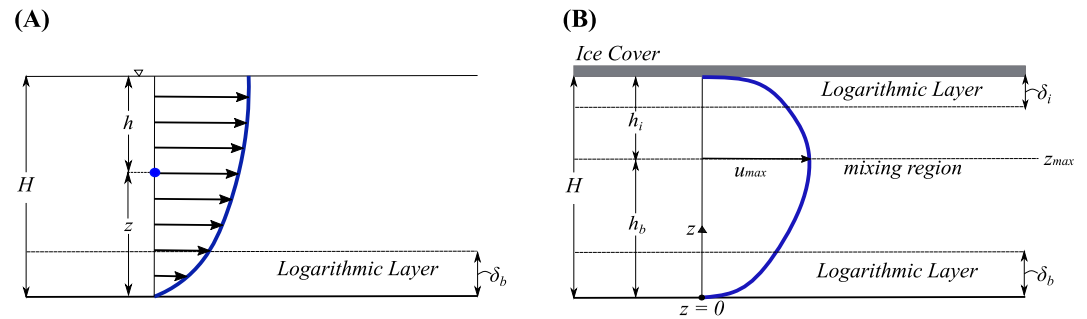
Figure 1. The differences in flow configuration under (a) open-surface condition, and (b) ice-covered condition. Under open-surface condition, the total depth $H = h + z$ is separated into two portions: (i) the distance to the river bed (z) of a measured point; and (ii) its local depth (h). Under ice-covered condition, two logarithmic layers are assumed near the ice layer (δ_i) and the river bed (δ_b). The z_{max} is the position of the maximum velocity (u_{max}) from the river bed.

configuration has been well studied under laboratory conditions (Hanjalić & Launder, 1972) in which the aspect ratio (width/depth) has been shown to control the overall flow dynamics.

There has been no universal law for asymmetrical flow configuration in rivers. In contrast to the logarithmic law of the open-surface case, it is unclear on the form of the time-averaged velocity profile in the asymmetrical configuration (Guo et al., 2017). There exists a maximum velocity, which typically does not locate on the symmetry plane (Tatinclaux & Gogus, 1983; Tsai & Ettema, 1994b; Urroz & Ettema, 1994b). As the shape of the velocity profile is changed under ice-covered condition, its gradient near the river bed is different from the open-surface counterpart (Guo et al., 2017). Therefore, the hydraulics of ice-covered flows differs significantly (Ettema, 2002; Prowse, 2001a) from the open-surface condition.

The main structure of the velocity profile can be described in Figure 1. We denote z as the distance from a measured point to the river bed surface as shown Figure 1a. The vertical distance corresponding to the maximum velocity u_{max} is z_{max}. Under ice-covered condition, z_{max} separates the entire profiles into: (a) the ice layer (h_i); and (b) the bed layer (h_b) as shown in Figure 1b. Thus the total depth $H = h_i + h_b$. Note that the local depth of a measured point is $h = H - z$. The stationary boundary condition on the ice and the bed surface dictate that $u(z = 0) = u(z = H) = 0$.

Under open-surface condition, one fundamental quantity that characterizes velocity profile near the river bed (Wilcock, 1996) is the friction velocity ($u_b^\star$). It can be linked to the bed shear stress as $\tau_b = \rho \left(u_b^\star \right)^2$, which is needed to determine sediment transport processes (Chaudhry, 2007). Therefore, the evaluation of $u_b^\star$ and τ_b are frequently required in river hydraulics.

Direct measurement of the bed shear stress τ_b or shear velocity $u_b^\star$ in rivers is not feasible (Petrie & Diplas, 2016) with the current technologies. Thus many methods have been proposed (Biron et al., 1998) to calculate $u_b^\star$ indirectly from velocity measurements. Since the flow in the alluvial channel is characterized by high Reynolds numbers, turbulent statistics are typically involved in the calculation of $u_b^\star$ (A. Sukhodolov et al., 1999): (a) Turbulent Kinetic Energy (TKE) (Soulsby, 1981), (b) Reynolds stress, and (c) Wall similarity methods (Hurther & Lemmin, 2000; López & García, 1999). These methods are highly accurate and they do not assume a predetermined velocity profile. However, they require the full calculation of the Reynolds stress tensor. Therefore, precise measurement of turbulent fluctuation u' is required along the water column pointwisely. For a small or medium river (A. Sukhodolov et al., 1999), it is a tedious task to perform this type of measurement along a cross-section in a reasonable amount of time because the sensor needs to traverse systematically point-to-point. For a large river, it is not feasible to carry out such a field campaign due to the potential change of the hydrological conditions (water level and discharge), which might alter completely the turbulent regime. Thus these methods are not widely used under field conditions.

The most common method to determine $u_b^\star$ in practice is to utilize the time-averaged velocity profile to determine $u_b^\star$ via the assumption of a logarithmic layer close to the river bed (Biron et al., 1998; Petrie & Diplas, 2016; Petrie et al., 2013). The main assumption is that there exists an equilibrium layer near the river bed at which the turbulence production and dissipation balances out to give rise to the logarithmic law. In

zero pressure gradient, the universal law of the wall has been verified in many laboratories and numerical simulations (Volino & Schultz, 2018). This logarithmic method does not require the acquisition of highly resolved turbulent statistics (Biron et al., 1998) and thus this procedure can be applied for many types of measurement devices including the popular Acoustic Doppler Current Profiler (ADCP) (Muste, Yu, Pratt, & Abraham, 2004; Muste, Yu, & Spasojevic, 2004; Petrie & Diplas, 2016). Since ADCP can provide the entire velocity profile in the water column in one measurement, the sensor is kept afloat at a stationary location (fixed-vessel method) (Petrie & Diplas, 2016) for a period, which can vary from 1 to 25 min (Petrie et al., 2013). The time-averaged velocity profile is then fitted with the logarithmic law to find $u_b^\star$. Note that due to the spatial averaging nature, the ADCP data cannot be represented using a prefixed confidence limit (Petrie & Diplas, 2016; Petrie et al., 2013).

In order to compute shear velocities for ice-covered flows (A. Sukhodolov et al., 1999), it has been hypothesized (two-layer hypothesis) that there exist three regions: (a) two logarithmic layers near the river bed and the ice surface; and (b) the mixing (core) region at the mid-depth as shown in Figure 1b. Here, two logarithmic layers are assumed to locate near the top (ice) and bottom (river bed) surfaces. Using the two-layer hypothesis, the logarithmic law method is typically applied (Ghareh Aghaji Zare et al., 2016) separately within the ice layer (δ_i) and the bed layer (δ_b) as shown in Figure 1b. To resolve the logarithmic layers, it is required that measured data must be carried out at locations near the ice layer and the river bed (A. Sukhodolov et al., 1999). However, the validity of the two-layer hypothesis has been questioned (Urroz & Ettema, 1994a) in meandering rivers since the secondary flows (Demers et al., 2011) might alter the local velocity profiles. In addition, it has been pointed out (Guo et al., 2017) that the double log-law profile is not physical as it is not possible to satisfy the continuity condition at the maximum velocity location u_{max}. This challenge motivates the use of the entire velocity profile (Attar & Li, 2012) to derive $u_i^\star$ and $u_b^\star$ in ice-covered flows. This practice alleviates the requirement of resolving the logarithmic layer but it needs an assumption on the form of velocity distribution, which is generally not known under the field condition. To provide a physical argument for assuming the velocity profile (Guo et al., 2017), have derived an analytical form of velocity distribution along the water column using an assumption on the distribution of eddy viscosity. However, the accuracy and reliability of this method in estimating $u_i^\star$ and $u_b^\star$ (Guo et al., 2017; F. Wang et al., 2020) has not been examined in river bends.

As the logarithmic layer is considered valid within a thickness of (δ_b) in the bed layer as elaborated in Figure 1b, it is common to use wall units to non-dimensionalize hydraulic quantities. In this approach, $u_b^\star$ and ν are used to form the velocity and viscous length scales. The friction Reynolds number based on shear velocity $\left(u_b^\star\right)$, the logarithmic layer thickness δ_b, the vertical distance from the river bed z, and the non-dimensional velocity profile $u^+(z^+)$ are expressed in terms of wall units as:

$$
\begin{aligned}
Re_\tau^b &= \frac{H u_b^\star}{\nu} \\
\delta_b^+ &= \frac{\delta u_b^\star}{\nu} \\
z^+ &= \frac{z u_b^\star}{\nu} \\
u^+(z^+) &= \frac{u(z)}{u_b^\star}
\end{aligned}
\tag{1}
$$

Under laboratory condition, the logarithmic layer δ_b^+ can extend (Guo et al., 2017) up to $z^+ = 10^4$.

A similar procedure can be carried out to define the shear velocity for the ice layer as seen in Figure 1b with the shear velocity $\left(u_i^\star\right)$:

$$
\begin{aligned}
Re_\tau^i &= \frac{H u_i^\star}{\nu} \\
\delta_i^+ &= \frac{\delta_i u_i^\star}{\nu} \\
h^+ &= \frac{h u_i^\star}{\nu} \\
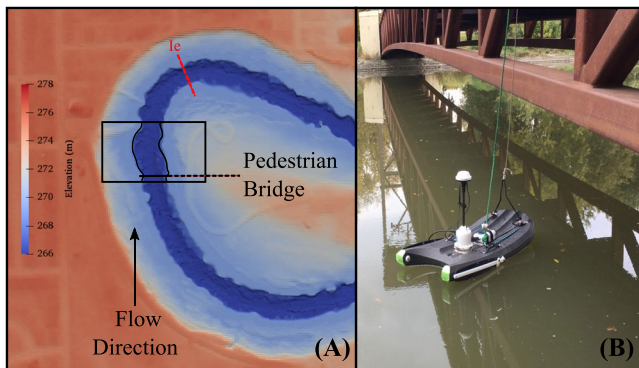u^+(h^+) &= \frac{u(h)}{u_i^\star}
\end{aligned}
\tag{2}
$$

Figure 2. The study area and the measurement cross-sections. (a) The area of interest at the apex of a bend, and the location of cross-section *Ie*. The flow is in the North direction. (b) Under open-surface condition, the ADCP M9 sensor is deployed near the pedestrian bridge with the fixed-vessel methodology in five measurement days *Oa*, *Ob*, *Oc*, *Od*, and *Oe* (see Table 1). On each measurement day, the *M*9 is stationed in a number of vertical locations across the bridge as shown in Table 1.

Under open-surface condition, the existence of the logarithmic layer has been assumed to follow the theoretical estimate (Gao et al., 2020) as:

$$2.6 Re_\tau^{1/2} \leq z^+ \leq 0.15 Re_\tau \tag{3}$$

The upper bound (thickness) for the logarithmic layer is thus: $\delta_{theory}^+ = 0.15 Re_\tau$.

To date, there has been no report on the thickness of the logarithmic layer under ice-covered condition.

As mentioned above, one important factor affecting the distribution of $u_b^\star$ is the effect of secondary flows (Petrie & Diplas, 2016). Laboratory experiments (Anwar, 1986) have shown that the vertical velocity profile deviates from the logarithmic law in the bend region. In complex three-dimensional flows, it is even not possible to derive $u_b^\star$ using the logarithmic hypothesis (Biron et al., 2004). The distribution of the bed shear stress (τ_b) and thus the shear velocity $(u_b^\star)$ has been shown to be dependent on the local secondary flows (Bathurst et al., 1979; Stoesser et al., 2010). Since the understanding of secondary flows under ice-covered condition is limited, it is unclear how ice cover impacts the velocity and shear velocity distribution in meandering rivers. In a laboratory experiment (Urroz & Ettema, 1994a) has shown that there exists two counter-rotating vortices (double-stacked cell) in the secondary flow pattern of an ice-covered bend. These two vortices are thought to belong to a complex three-dimensional structure of the bend flow. Field measurements of (Demers et al., 2011) suggests that this double-stacked cell appears near the bend entrance but diminishes rapidly toward a single helical cell at the bend apex.

The main goal of the current study is to examine the impact of ice coverage on the vertical flow profile and its implication on the cross-stream distribution of bed shear stress. Field works are carried out under both open-surface and ice-covered conditions to provide the vertical velocity profiles. Whenever appropriate, the logarithmic law is invoked to derive $u_b^\star$ and $u_i^\star$. On the other hand, the applicability of the quartic solution (Guo et al., 2017) will be examined using our measured data set. The results from these methods are compared to evaluate their compatibility in providing accurate value of shear velocities. The three-dimensional structures of flows under ice coverage are also discussed to identify locations where complex flow patterns might occur and limit the use of analytical methods.

2. Methodology

2.1. Study Area

Red River is known as a low-gradient river with its regular basis Spring floods. The channel bed of the Red River is mostly categorized as clay and fine silt (Weiss et al., 2015). A 2-km long section of the Red River near Lindenwood Park in Fargo, North Dakota was decided as the study field (Figure 2a). A pedestrian bridge located in the middle of the apex served as the reference location (Figures 2a and 2b). At the end of the reach, there exists a United States Geological Survey (USGS) station (USGS FARGO 09020104) at the gage elevation of 262.68 m above the North American Vertical Datum (NAVD88).

2.2. Measurement Methodologies

Following the suggestion of (A. N. Sukhodolov, 2012; A. Sukhodolov et al., 1999), the fixed-vessel (FV) method (Petrie et al., 2013) was used for this study. The Acoustic Doppler Current Profiler (ADCP), Sontek *M*9, was used to measure the velocity components and bathymetry under the SmartPulse mode of 1 MHz. Note that the compass calibration must be carried out prior to each measurement. In our measurement, the blank distance was set to be 0.05 m. The measured bin was adjusted automatically and varied from 0.02 to 0.06 m depending on the total depth H ($H_{max} \approx 4.1$ m). Bin size at each vertical is monitored in the entire time series. Any time instances that have changes in the value of bin size are removed from the calculation. The signal-to-noise ratio (SNR) of all measurements were monitored online during the campaigns and also examined after the acquisition to check their reliability to avoid beam separation. The presence of signal interference near the river bed ($z \leq 30$ cm) was

Table 1
Expeditions in Fall 2020 Winter 2020 and 2021, and Summer 2021

Case	Date	Surface	Q (m³/s)	Elevation (m)	No. verticals	T_∞ (mins)
Oa	Oct/02/20	Open	23.41	265.96	13	10
Ob	Oct/04/20	Open	23.87	265.96	12	10
Oc	June/22/21	Open	14.30	265.87	8	15
Od	June/24/21	Open	12.20	265.85	11	15
Oe	June/30/21	Open	6.82	265.72	6	15
Ia (M1/M2)	Feb/19/21	Ice	12.5	265.92	6	2
Ib (M1/M2)	Feb/20/21	Ice	12.8	265.92	7	2
Ic	Feb/21/21	Ice	13.8	265.93	7	2
Id	Feb/21/21	Ice	13.8	265.93	8	2
Ie (M1/M2)	Feb/21/21	Ice	13.8	265.93	6	2

Note. The hydrological data (flow discharge Q and elevation) is monitored at the USGS Fargo (09020104) Station. The exact location of each vertical location is illustrated in Figure 13. T_∞ (minutes) is the total time of measurement in each vertical/ (ice hole) location. The notations $M1$ and $M2$ denote two consecutive measurements in one ice hole.

significant, thus the SNR was monitored closely in this region. If the SNRs from four different sensors were different from each other by 20 dB, the data points were omitted from the calculations.

Under open-surface condition, only one cross-section was chosen at the bridge location (see Figure 2a) (*O*) since it was a well-defined cross-section (red line). Measurements under open-surface condition were carried out on five measurement campaigns: (a) 2 October 2020 (*Oa*), (b) 4 October 2020 (*Ob*), (c) 22 June 2021 (*Oc*), (d) 24 June 2021 (*Od*), and (e) 30 June 2021 (*Oe*). The *M*9 was attached to a Sontek Hydroboat as shown in Figure 2b. The fixed-vessel deployment technique was implemented by taking advantage of the pedestrian bridge. The location of the sensor (*M*9) was monitored both using the on-board GPS as well as the marked locations in the bridge section. As the HydroBoat is attached to the pedestrian bridge, its lateral motion is kept minimal. Our on-board GPS data shows a variation of 0.35 m in the lateral position of the boat, which is at the accuracy limit of the GPS device. At each vertical location, the *M*9 was kept stationary for at least 600 s. The value of (ℓ) indicated the distance from the outer bank along the horizontal axis X as shown in Figure 4a. The details of measurements and their associate discharges are shown in Table 1.

Under ice-covered condition, measurements were conducted by opening ice holes (Figure 3b). The number of opened ice holes varied from 6 to 8 holes depending on the cross-section. Locations of the ice holes were measured from the outer (left) bank. In order to probe the three-dimensional flow structures at this location, four separate cross-sections were chosen for measurements to elucidate the three-dimensional flow structures: *Ia* (19 February 2021), *Ib* (20 February 2021), *Ic* (21 February 2021), and *Id* (21 February 2021). These cross-sections were separated by a distance of 6.1 m along the North (*Y*) direction. To avoid bias in the measurement, a separate cross-section *Ie* (21 February 2021) at the bend apex, which was 310 m away from the bridge, was selected for an additional measurement (Figure 2a). In each measurement, the Sontek *M*9 sensor was placed 0.2 m under the ice layer. The distance from left bank ℓ at each cross-section was noted during the field survey and represented for each cross-section as seen in the diagram of Figure 3b. The period of measurement was limited to 120 s to avoid freezing of the equipment's surface since the air temperature went below −20°C. This low air temperature was to ensure that the ice thickness was at least 0.25 m, which was required to be safe to perform measurements. All details of the measurements were summarized in Table 1.
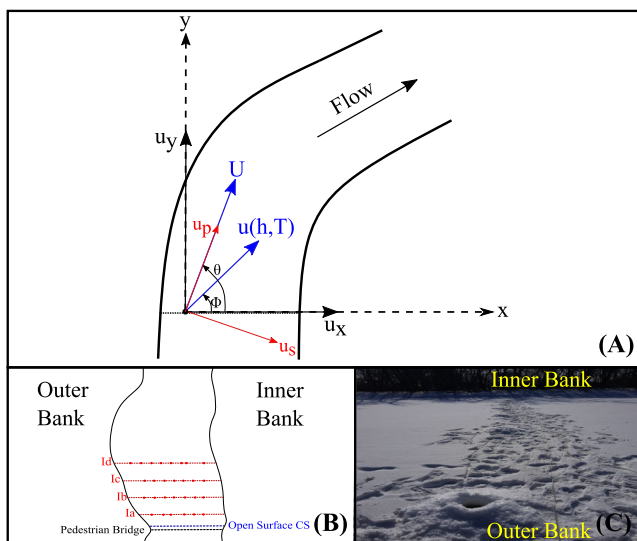

Figure 3. (a) The schematic diagram of the Rozovskii method. The degree of ϕ represents the orientation of time-averaged velocity, and θ is the degree of the depth-averaged velocity to the positive x axis. (b) The diagram shows the ice holes in five consecutive cross-sections *Ia*, *Ib*, *Ic*, *Id* and *Ie* in February 2021. The number of ice holes for each cross-section is shown in Table 1. Each vertical location in one cross-section is marked by its distance from the corresponding left bank ℓ (m) (see also Figure 4). (c) Cross-sectional view of the river and ice holes next to the pedestrian bridge (19 February 2021).
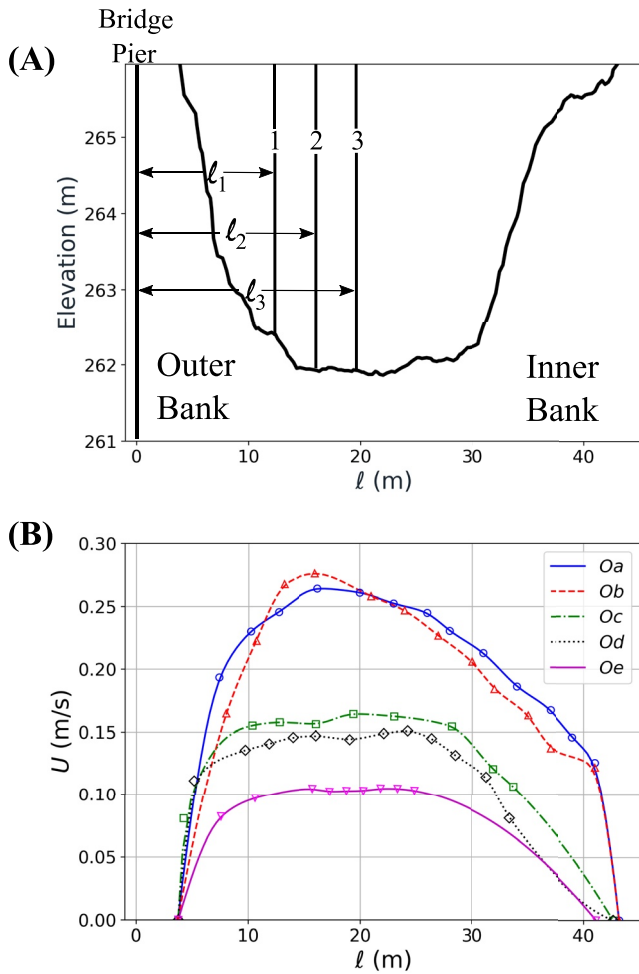
(A)

(B)

Figure 4. The depth-averaged velocity profiles (U) under open-surface condition at the bend apex. (a) The cross-section shape at the bridge. The value ℓ denotes the distance of the vertical location to the left bank. (b) Depth-averaged velocity profiles under different flow discharge Oa, Ob, Oc, Od, and Oe. The thalweg is defined as area with the total depth $H \geq 3.5$ m, which is in the $10\ m \leq \ell \leq 30$ m region for this cross-section.

2.3. Data Processing and Flow Statistics

The raw data of the M9 in text format were processed using our in-house MATLAB code to produce 1 Hz time series. A separate MATLAB code was used to calculate flow statistics from the time series including: (a) the depth-averaged velocity profiles; and (b) the time-averaged velocity profile for each vertical location. Following the suggestion of (Petrie & Diplas, 2016), the depth-averaged value $U(T)$ and the time-average profiles for each vertical $u(z, T)$ were computed as the function of averaging period T as:

$$U(T) = \frac{1}{H} \int_{z=0}^{z=H} u(z,T) dz \tag{4}$$

$$u(z,T) = \frac{1}{T} \int_{t=0}^{t=T} u(z,t) dt \tag{5}$$

The final values of $U(T_\infty)$ and $u(z, T_\infty)$ correspond to the time-averaged value of the entire record ($T = T_\infty$). They are denoted as the long-term depth-averaged (U_∞) and time-averaged ($u_\infty(z)$) velocities, respectively, to provide a scale to indicate the range of variability of the signals. Note that our notation to describe the long-term (average) values are consistent with ones proposed by (Petrie & Diplas, 2016). Under the open-surface condition, the total length of the measurement period T_∞ for each vertical was $T_\infty \geq 10$ min whereas it was only $T_\infty \approx 2$ min for ice-covered cases as shown in Table 1. In total, there were 50 and 55 depth-averaged time series under the open-surface and ice-covered conditions, respectively. Finally, the calculation of the shear velocity $u_b^\star$ and $u_i^\star$ was based on the values of $u_\infty(z)$ as shown in the next sections. All subsequent analyses are conducted based on the time-averaged (u_∞) and depth-averaged (U_∞) velocity.

2.4. The Logarithmic Law of the Wall

The logarithmic law of a rough wall (Shen & Lemmin, 1997) is:

$$\frac{u(z)}{u_b^\star} = \frac{1}{\kappa} \ln \frac{z}{z_0} + \beta \tag{6}$$

where $\kappa = 0.39$ is the Von Karman constant, β is the additive constant ($\beta = 8.5$). The parameter z_0 is the roughness length. The range of von Karman constant is $0.39 \leq \kappa \leq 0.41$ (Biron et al., 1998; Marusic et al., 2013; Petrie & Diplas, 2016; Petrie et al., 2013). The value of $\kappa = 0.39$ is selected as the condition of high Reynolds number flows in rivers (Marusic et al., 2013). In natural rivers, this logarithmic law is typically considered valid within a distance δ_b from the river bed. Typically, δ_b varies from 20% to 50% (Petrie & Diplas, 2016; Petrie et al., 2013) of the total depth H. Under field conditions, the value of δ_b is not known in advance. Therefore, a procedure to determine δ_b will be discussed below.

The shear velocity $\left(u_b^\star\right)$ and the roughness length (z_0) are found by fitting the Equation 6 with the measured data ($u(z)$) in each vertical. A common procedure (Petrie & Diplas, 2016) is to use the linear regression line between the measured value of $u(z)$ and $\ln(z)$. As the linear regression line is known, the values of $u_b^\star$ and z_0 are computed as:

$$u_b^\star = \kappa m \tag{7}$$

$$z_0 = \exp\left[8.5\kappa - \frac{\gamma}{m}\right] \tag{8}$$

Here, γ and m are the intercept point and the slope of the best-fit regression line, respectively.

Under open-surface condition, the agreement between the linear regression line and the measured data must satisfy (Petrie & Diplas, 2016) the following criteria: (a) the correlation coefficient $R^2 > 0.9$, (b) a positive shear velocity $u_b^\star > 0$, and (c) a realistic value of z_0 (0.001 $m < z_0 < 10$ m). In brief, the detailed steps of the logarithmic method for both open-surface and ice-covered conditions are as follows:

- *Step* 1: Assume a value of δ_b ranging from 0.05 to 1.0 H with an increment of 0.05 H for each trial. The fitting to the logarithmic law is performed only when there is sufficient data in the logarithmic layer δ_b. The presence of at least five points within δ_b is required.
- *Step* 2: The velocity magnitude $u(z)$ is plotted against the $\ln(z)$ at every measurement point. Available MATLAB functions, "*polyfit*" and "*polyval*" are called to perform linear regression from the selected points in Step 1, to obtain the linear fitting parameters m and γ.
- *Step* 3: The shear velocity is computed as $u_b^\star = \kappa m$.
- *Step* 4: Equation 8 is used to compute the roughness length (z_0) using the values of the parameters γ and m.
- *Step* 5: R^2 value is computed from the linear fitting of Equation 6 in comparison to the corresponding measured data. The values of R^2, $u_b^\star$, and z_0 are checked simultaneously to validate the presence of the logarithmic layer. The following values are validated with $R^2 > 0.9$, $u_b^\star > 0$, and 0.001 $m < z_0 < 10$ m.
- *Step* 6: Record the value of R^2 and δ_b. Go back to Step 1 with an increment in the value of δ_b until the best R^2 is found. If the best R^2 is greater than 0.9, move to Step 7.
- *Step* 7: Compute $u_b^\star$ and its associated z_0 corresponding to the best R^2.

The logarithmic fitting is performed for the ice layer in a similar fashion using the non-dimensional distance to the ice layer h^+ as shown in Equation 2.

2.5. Quartic Profile for Asymmetrical Flows

The quartic profile of (Guo et al., 2017) is formulated using the relative distance η, which is defined as $\eta = 2\frac{z}{H}$. The maximum velocity location is defined in term of its relative distance as: $\eta_{max} = \frac{2z_{max}}{H}$.

A non-dimensional parameter (λ) is used to represent the asymmetry of the flow profile as:

$$\lambda = \sqrt{\frac{2}{\eta_{max}} - 1} \tag{9}$$

Here $\lambda = \frac{u_i^\star}{u_b^\star}$ quantifies the asymmetry of shear stress on the top $\left(u_i^\star\right)$ and bottom $\left(u_b^\star\right)$ surfaces. Therefore, the value of λ is important in determining the shape of the velocity profile. An interim parameter $\left(\alpha = \frac{1-\lambda}{\lambda - \lambda^{2n}}\right)$ is also used to reflect this asymmetry. In this equation, n is the mixing turbulent intensity. While n can vary depending on the turbulent flow condition, it is found for the symmetric flow condition as $n = 5/6$ (Guo et al., 2017).

The location of the zero shear stress plane (η_c) typically does not coincide (Hanjalić & Launder, 1972) with the maximum velocity location. After the value of λ is obtained from the Equation 9, the value of η_c is computed as:

$$\eta_c = \frac{2}{(1 + \lambda^n)} \tag{10}$$

Since λ is close to 1, the values of the critical and maximum positions are typically close in the thalweg ($u_c \approx u_{max}$, $\eta_c \approx \eta_{max}$).

The quartic solution finds the best fit velocity profile (u_f) to the measure data. u_f can be written in terms of its non-dimensional form u^+ with the help of the bed shear velocity $u_b^\star$ as:

$$\frac{u_f(\eta)}{u_b^\star} = u^+(\eta) \tag{11}$$

Therefore, the bed shear velocity is used to provide a non-dimensional profile $u^+ = u/u_b^\star$. For example, the critical velocity at the critical depth η_c is non-dimensionalized as $\left(u_c^+ = u_c/u_b^\star\right)$.

The main contribution of (Guo et al., 2017) is that the dimensionless velocity profile (u^+) is suggested to follow the analytical solution:

$$u^+(\eta) = u_c^+ + \phi(\eta) \tag{12}$$

Here the velocity profile function ($\phi(\eta)$) is derived for infinitely long and straight channel as:

$$\phi(\eta, \lambda) = \frac{1}{\kappa} \left\{ \ln\left(\frac{\eta}{\eta_c}\right) + \lambda \ln\frac{2-\eta}{2-\eta_c} - \frac{1+\lambda}{2} \ln\left[1 + \alpha\left(1 - \frac{\eta}{\eta_c}\right)^2\right] \right.$$
$$\left. - \left(1 - \lambda^{n+1}\right)\sqrt{\alpha}\tan^{-1}\sqrt{\alpha}\left(1 - \frac{\eta}{\eta_c}\right) \right\}$$

(13)

The shear velocity at the river bed can be calculated as:

$$u_b^\star = \frac{\sum_j \phi(\eta_j, \lambda)(u_j - u_c)}{\sum_j \phi^2(\eta_j, \lambda)}$$

(14)

Our detailed steps for fitting the vertical velocity profile under the ice-covered condition with the ADCP data are as follows:

- *Step* 1: In each vertical location, the entire measurement points are selected from the value of $u(z)$ as discussed in Section 2.3. The number of available points along the depth is dictated by the measured cell size ($0.02 - 0.06$ m), which is automatically adjusted by the $M9$ sensor. Note that in each cross-section Ia, Ib, and Ie, there are two separate measurements $M1$ and $M2$ (2 min each) at every vertical location (see also Table 1). In such cases, the fitting procedure is performed on the averaged value of $M1$ and $M2$. Since the number of points along the depth can be slightly different between the first measurement $M1$ and the second measurement $M2$, we need to reconstruct the averaged profile of $M1$ and $M2$. First, the distance z is converted into the relative distance ($0 \leq \eta \leq 2$). The value of the entire depth is then divided into uniform intervals $N = 100$ in each vertical location as η_i ($i = 1 \rightarrow N$). For each measurement $M1$ or $M2$, a procedure is carried out to map the measured data $u(z_i)$ into the interpolated value $u(\eta_i)$ at the location η_i using the MATLAB function, *"interp1"* with piecewise cubic spline interpolation. Second, the averaged value of $\bar{u}(\eta_i)$ between the measurement $M1$ and $M2$ is finalized for further processing.
- *Step* 2: To further smooth out the variation of $\bar{u}(\eta_i)$ long the depth, a Fourier filtering method is performed on $\bar{u}(\eta_i)$ with the first 5 frequencies to obtain the filtered value $\widetilde{u(\eta_i)}$.
- *Step* 3: The location of the maximum velocity $\widetilde{u_{max}}$ in the vertical axis (η_{max}) is identified in this step. Since the value of η_{max} controls the fitting accuracy, it is important to investigate the sensitivity of the fitting procedure with η_{max} systematically. The value of η_{max} is varied within the 10% range.
- *Step* 4: The parameters λ and α are computed according to Equation 9 with the chosen value of η_{max}. The location of the critical position of the eddy viscosity (η_c) is computed from the Equation 10. To reduce the sensitivity of the fitting to process to the selection of η_{max}, the critical velocity is set to be equal to the maximum velocity $\left(u_c = \widetilde{u_{max}}\right)$.
- *Step* 5: The velocity distribution function ($\phi(\eta_i)$) is computed by Equation 13.
- *Step* 6: The shear velocity at the river bed $u_b^\star$ is computed by Equation 14 using the values of $\tilde{u}_i$ and u_c. The non-dimensional critical velocity is computed as $u_c^+ = \frac{u_c}{u_b^\star}$.
- *Step* 7: The non-dimensional velocity profile ($u^+(\eta_i)$) is produced by Equation 12.
- *Step* 8: The fitted velocity magnitude ($u_f(\eta_i)$) at the depth η_i is computed by Equation 11.
- *Step* 9: The correlation coefficient factor R^2 between the measured ($u(z)$) and fitted ($u_f(z)$) velocity profiles is computed. Record the dependence of the value R^2 on η_{max}.
- *Step* 10: Go back to Step 3. The iterative process will terminate until the highest correlation value R^2 is obtained with the selected η_{max}.

The fitting error is calculated using the RMSE criterion as follows:

$$RMSE = \sqrt{\frac{\sum_j^n (u_j - u_m)}{N_{obs}}}$$

(15)

Here, N_{obs} stands for number of observations along the depth while u_m is the corresponding value on the fitting curve.

2.6. Estimation of $u_b^\star$ From Depth-Averaged Velocity (Friction Method)

The computation of boundary shear stress is a challenge since the ADCP is not able to measure accurately the flow velocities near the river bed due to the side-lobe interference. This challenge leads to the use depth-averaged

velocity vector $\vec{U}(U_x, U_y)$ (Engel & Rhoads, 2016) to estimate $u_b^\star$ under open-surface condition. The procedure is as follows:

$$C_f = \left[\alpha_r \left(\frac{H}{z_0} \right)^{\frac{1}{6}} \right]^{-2}$$

$$\tau_{bx} = \rho C_f U_x \sqrt{U_x^2 + U_y^2}$$

$$\tau_{by} = \rho C_f U_y \sqrt{U_x^2 + U_y^2} \quad (16)$$

$$\tau_b = \sqrt{\tau_{bx}^2 + \tau_{by}^2}$$

$$u_b^\star = \sqrt{\frac{\tau_b}{\rho}}$$

where, ρ, C_f, and z_0 are the fluid density, the friction coefficient, and the roughness height, respectively. The coefficient α_r is set equal to 8.1 (Parker, 1991). The equivalent roughness height z_0 is estimated as $2.95 \times d_{84}$ (Whiting & Dietrich, 1990). The sediment characteristics of the Red River at Fargo have been well studied (Galloway & Nustad, 2012) by the United States Geological Survey (USGS). The particle-size distribution of the study area indicates that fine particle (silt) is the most commonly found in the study area. The distribution shows that $d_{50} = 0.5$ mm. The value of d_{84} is computed from the USGS field survey data as $d_{84} \approx 2.088$ mm (Blanchard et al., 2011; Galloway & Nustad, 2012). U_x and U_y are the two components of the depth-averaged velocity vector $\left(\vec{U} \right)$ along the X and Y, respectively. The corresponding components of the magnitude shear stress (τ_b) are defined as τ_{bx} and τ_{by}. Since the depth-averaged velocity $\vec{U}$ is available for all vertical locations, this friction method can be applied anywhere. The Equation 16 indicates a direct correlation between $u_b^\star$ and U (Chauvet et al., 2014). The advantages and disadvantages of the logarithmic, quartic, and friction methods for computing shear velocity will be compared and contrasted.

2.7. Secondary Flow Visualization

The classical Rozovskii's method (Lane et al., 2000) is used to visualize the secondary flow pattern as shown in Figure 3a. The Cartesian components of the velocity u_x (East), u_y (North), and u_z (up) are used to derive the secondary components. The primary and the secondary flow components are u_p and u_s are computed using the projections of the East and North components on the depth-averaged velocity vector at the vertical:

$$u_p = \left(u_x^2 + u_y^2 \right)^{0.5} \cos(\theta - \phi) \quad (17)$$

$$u_s = \left(u_x^2 + u_y^2 \right)^{0.5} \sin(\theta - \phi) \quad (18)$$

Here ϕ and θ are defined as the angle between the depth-averaged vector U and the time-averaged vector u to the x (East) direction in the counter-clockwise direction. The components u_s and the u_z are used to visualize the secondary flow pattern.

3. Result

As the measured cross-sections locate in a meandering bend, the impact of the channel curvature is significant. This effect is presented using the depth-averaged velocities U under open-surface condition as shown in Figure 4. Overall, the depth-averaged profiles are asymmetrical toward the outer bank. At high discharges (Oa and Ob), the maximum velocity is visible in the left part of the thalweg. Note that $Q_{Oa} \approx Q_{Ob}$ and thus the velocity profiles of Oa and Ob are closely similar. At low flow conditions (Oc, Od, and Oe), such an asymmetry is not distinct as the flow in the thalweg is nearly uniform. In the following sections, the characteristics of the vertical profiles will be examined at each location ℓ in the cross-sections. First, the statistical analysis is carried out to determine if the measured data is sufficient to generate reliable values for U and $u(z)$. Second, the validity of the logarithmic law is examined under open-surface condition. Third, the presence of the double log-law is investigated for the ice-covered cases. Fourth, we revisit the quartic solution and its applicability to derive shear velocity for

ice-covered condition in the current study. Finally, we address the changes in secondary flow patterns under the impacts of the ice cover.

3.1. Data Statistics

Under open-surface condition, the results show that the value of the time-averaged velocity $u(h, T)$ at all locations h along the depth does depend on the averaging period T. Figure 5 illustrates that the $u(h, T)$ mostly oscillates near the free surface ($h = 0.26$ m) and the bed ($h = 3.44$ m) at the stations of Oa_5 and Ob_5, especially when $T < 200$ s. Despite the continuous oscillations even after the $T = 200$ s, they remain in the 5% of u_∞ range. In particular, $u(h, T)$ converges to its long-term values $u_\infty(h)$ within $\pm 5\%$ in the first 100 s. The value at the mid-depth $u(h = 1.82$ m,T) converges even more quickly to the long-term value. In contrast to the time-average velocity, the depth-averaged $U(T)$ converges rapidly to its long-term value U_∞ without any significant oscillation within the first minute. As shown in Figure 4, the obtained depth-averaged profiles of Oa and Ob are consistent given closely similar flow discharges. A similar observation is applied for Oc and Od. In brief, the period $T \approx 200$ s is sufficient for the time-averaged profile $u(h, T)$ and depth-averaged $U(T)$ to attain their accuracy within $\pm 5\%$ of their long-term values.

The variation of the vertical velocity profile $u(h, T)$ under different periods of averaging T is shown in Figure 6. To examine the convergence of the vertical profiles as a function of the period T, four different periods are selected: $D - 1$ ($t = 0 \rightarrow 120$ s) ; $D - 2$ ($t = 200 \rightarrow 320$ s); $D - 3$ ($t = 0 \rightarrow 400$ s); and $D - 4$ ($t = 0 \rightarrow 620$ s) for the verticals Oa_5 (Figure 6a) and Oc_6 (Figure 6b). In both Oa_5 and Oc_6, there exists a significant complex flow profile near the free surface ($h < 1.5$ m). In this region, the shape of the vertical profile is significantly dependent on the averaging period T. Comparing the period $D - 1$ and $D - 2$, which last 120 s, the time-averaged profiles ($u(h, T)$) are significantly different, especially in the near surface region. In the near bed region ($h > 2$ m), the shape of the profile is less sensitive to the choice of the period T. Indeed, the profile ($u(h, T)$) becomes nearly identical between $D - 3$ and $D - 4$ when the value of T is extended to 620 s. In other vertical locations, the convergence of velocity profiles is similar to ones as seen in Figure 6. Therefore, a period of 600 s (10 min) is sufficient to obtain the velocity profile convergence under open-surface condition.

The impacts of T value on the three-dimensional flow pattern can be examined using the East (u_E − x) and Up (u_{up} − z) components as shown in Figure 7 (the vertical Oa_8). Note that the magnitudes of u_E and u_{up} are one order of magnitude smaller than the u_N. Hence, any dependence of three-dimensional flow pattern on the duration T can be reflected easily in u_E and u_{up} components. Different values of T, which correspond to four subsets with different periods $D - 1$, $D - 2$, $D - 3$, and $D - 4$, are tested. As seen in Figure 7, the structure of the circulatory vortex is consistent across all averaging periods $D - 1$, $D - 2$, $D - 3$, and $D - 4$. Thus, the 10-min record ensures that the three-dimensional flow structure is captured accurately.

Under the ice-covered condition in Figure 8, the total length of the measurement period T_∞ is limited to approximately 120 s. Therefore, there exists a larger variation of $U(T)$ and $u(h, T)$ from their respective long-term values. As seen in Figure 8, two independent measurements ($M1$ and $M2$) of the same ice hole Ib_7 at the depth $h = 1.64$ m are shown. It can be seen that the ratios $\frac{U(T)}{U_\infty} \geq 10\%$ and $\frac{u(h,T)}{u_\infty(h)} \geq 20\%$ for both $Ib_7 - M1$ and $Ib_7 - M2$ at the early stage from $T = 0$ to $T = 100$ s. Here, it is seen that the stabilization of $u(h, t)$ and $U(T)$ can only attain when $T > 100$ s. For other ice holes, their running statistics also show a similar behavior. There exist a significant variation of $\frac{U(T)}{U_\infty}$ and $\frac{u(h,T)}{u_\infty(h)}$ within $\pm 10\%$ in the first minute. The values of $U(T)$ and $u(h, T)$ converge in a synchronous fashion only when $T > 100$ s. In brief, it is evident that the duration of measurement $T = 120$ s has a significant impact on the velocity profiles.

To examine the variability of the vertical profile due to a short period of measurement $T = 120$ s, the vertical profiles at the vertical Ib_7 in two consecutive measurements ($M1$ and $M2$) are plotted in Figure 9a. The results show that the overall vertical profiles of both measurements are consistent. However, the depth-averaged velocities are significantly different ($U_{M1} = 0.1591$ and $U_{M2} = 0.1967$ m/s). To further investigate the variation of the derived shear velocity, the logarithmic fitting is carried out for the bed and the ice layer in Figures 9b and 9c, respectively. There exists a significant difference in the value of $u_b^\star$ between the two measurements ($u_b^\star(M1) = 0.0352$ m/s and $u_b^\star(M2) = 0.0477$ m/s). However, the value of $u_i^\star$ does not vary significantly ($u_i^\star(M1) = 0.0269$ m/s and $u_i^\star(M2) = 0.0255$ m/s). Moreover, the separation from logarithmic profile initiates at $h^+ \approx 10, 251$ in the first
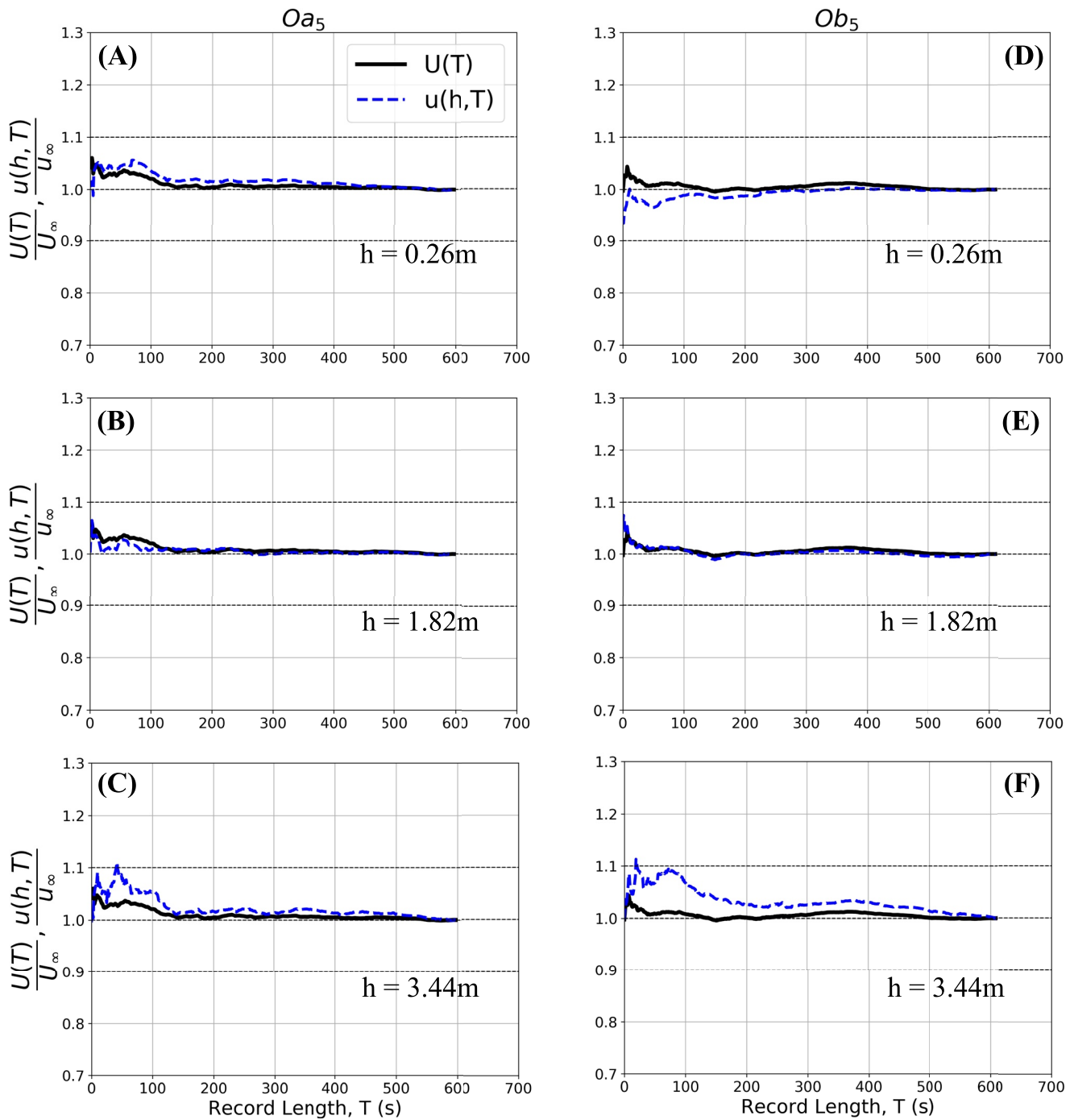
Figure 5. Statistical convergence properties for the depth-averaged velocity $U(T)$ and the time-averaged velocity $u(h, T)$ (Section 2.3) as the function of the record length T for the vertical location Oa_5 (left column—$H_{Oa_5} = 4.1$ m) and Ob_5 (right column—$H_{Ob_5} = 4.1$ m). The record length T is varied from 1 s to the entire record ($T_\infty \approx 600$ s). The long-term values of $U(T_\infty)$ and $u(h, T_\infty)$ are denoted as U_∞ and $u_\infty(h)$, respectively. Three values of depth are chosen $h = 0.26$ m (near surface), $h = 1.82$ m (mid-depth), and $h = 3.44$ m (near bed).

measurement ($M1$), while it is $h^+ \approx 9,693$ in the second measurement ($M2$). This behavior is consistent with the convergence characteristics as shown in Figure 8 where the two measurements exhibit slightly different convergence profiles. Recognizing this limitation, we use the averaged profile resulting from two measurements ($M1$ and $M2$).
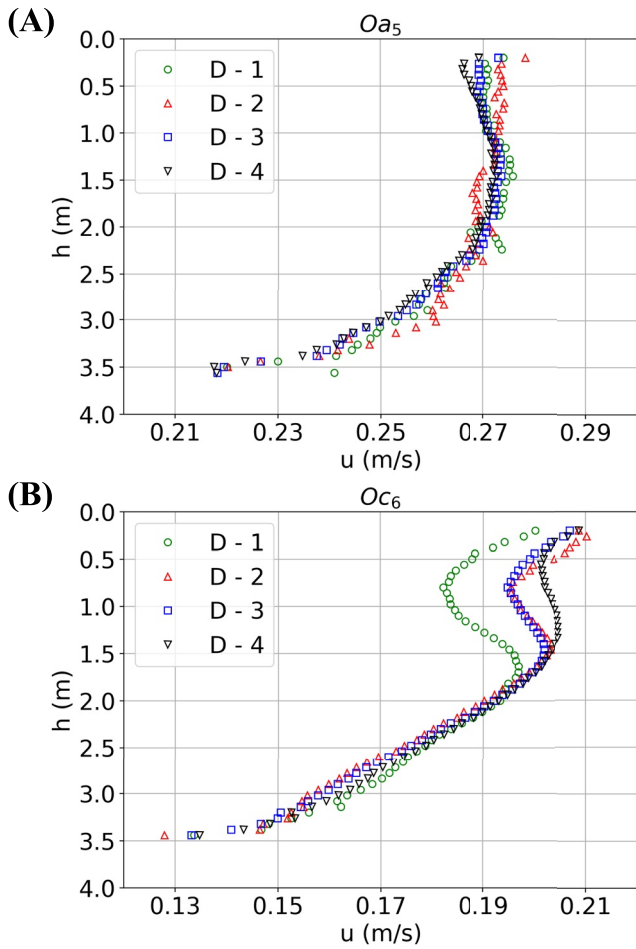
Figure 6. The variability of the vertical flow profile as the record length T changes at the vertical location Oa_5 and Oc_6. Four periods ($D-1$, $D-2$, $D-3$, and $D-4$) with different values of measurement period T (seconds) are examined: $D-1$ ($t = 0 \rightarrow 120$ s); $D-2$ $t = 200 \rightarrow 320$ s); $D-3$ ($t = 0 \rightarrow 400$ s; and ($D-4$) $t = 0 \rightarrow 620$ s. The vertical flow profile near the river bed converges rapidly in the first 120 s.

3.2. The Universality of the Logarithmic Law Under Open-Surface Condition

Under the open-surface condition, the logarithmic fitting is summarized in Table 2. The presence of the logarithmic law is validated in most measurements of Oa, Ob, Oc, Od, and Oe with high degree of agreement ($R^2 \geq 90\%$) in the thalweg. Location of each vertical is indicated under the column "ℓ (m)", as the distance from the outer bank. It can be observed in Table 2 that the logarithmic law is observed in all sufficiently deep locations ($H \geq 3.5$ m). In these locations, the logarithmic layer (δ_b) remains in 20% of the total depth ($\delta_b \approx 20\%H$). In the majority of the stations, the logarithmic layer can extend up to approximately 50% of the total depth. Therefore, the law of the wall is considered applicable for most locations in the bend thalweg regardless of the flow discharge.

To further examine the universality of the logarithmic law, the extension of the logarithmic layer is presented in Figure 10 in terms of wall units. Three vertical locations are shown in different measurement dates as Oc_4, Od_7, and Oe_5. The measured data fit excellently well with the logarithmic law as evidenced by the correlation between the $u^+(z^+)$ and z^+ for these cases in the range of $4,000 \leq z^+ \leq 10,000$. However, the separation from the logarithmic law initiates at different values of z^+ depending on the profile. For example, the separation starts at $z^+ \approx 15,000$ for the case Oc_4 and Oe_5. However, it starts much later at $z^+ \approx 20,000$ for the case Od_7. Here the value of the shear velocity $u_b^\star$ is found to vary around 0.01 m/s. Consequently, the local value of Re_τ^b (Equation 1) varies from 8,000 to 60,000. As shown in the Table 2, the logarithmic layer (δ_b^+) obeys the theoretical limit (Equation 3) excellently well with $\delta_b^+ \geq \delta_{theory}^+$ for all cases.

There are vertical locations that do not follow the logarithmic law (Oa_6, Oa_7, Oa_8, Oa_9, Ob_4, Oc_3). In these profiles, it is not possible to perform the logarithmic fitting with the listed constraints in Section 2.4. They are mostly located near the inner and outer banks where the secondary flows are strong. The deviation of the velocity profiles of these locations from the logarithmic law will be discussed in Section 3.5.

3.3. The Double Log-Law Under Ice-Covered Condition

In contrast to the open-surface condition, the presence of the logarithmic layer is found using the criteria in Section 2.4 only in limited locations near the bed as shown in Table 3. In those locations, the logarithmic layer δ_b extends well beyond 20% and up to 50% of H. Interestingly, the value of $u_b^\star$ is found to be significantly larger near banks $u_b^\star \approx 0.04$ m/s (Ib_7 and Id_8) than ones in the thalweg region (Ia_6, Ib_2, Ib_6, Ic_2, and Id_6) in which $u_b^\star$ varies around 0.01 m/s. In brief, our data confirm the presence of the logarithmic layer near the river bed in a limited number of ice holes.

The logarithmic layer near the ice cover is found in a larger number of vertical stations as shown in Table 4 in all cross-sections Ia, Ib, Ic, Id, and Ie. In these locations, the logarithmic layer extends mostly up to 20% of the total depth H in general. However, the value of the shear velocity $u_i^\star$ is generally lower than 0.01 m/s. In short, the applicability of the logarithmic law for the ice layer is different from the river bed layer.

Following the fitting procedure, lower and upper limits of $u^\star$ and z_0 are investigated using a 95% confidence limit as shown in Table 6 for both the ice and bed layers. On one hand, the results show that the confidence interval for $u^\star$ in bed and ice layers are in the order of 0.008 m/s, except verticals very close to the banks (e.g., Ia_1). On the other hand, the confidence interval of z_0 is unrealistically large in both ice and bed layers.

The thickness of the logarithmic layers in wall units (δ_i^+ and δ_b^+) for applicable ice holes are summarized in Tables 3 and 4 for the bed and the ice layer, respectively. Here, the theoretical bounds (Equation 3) are well
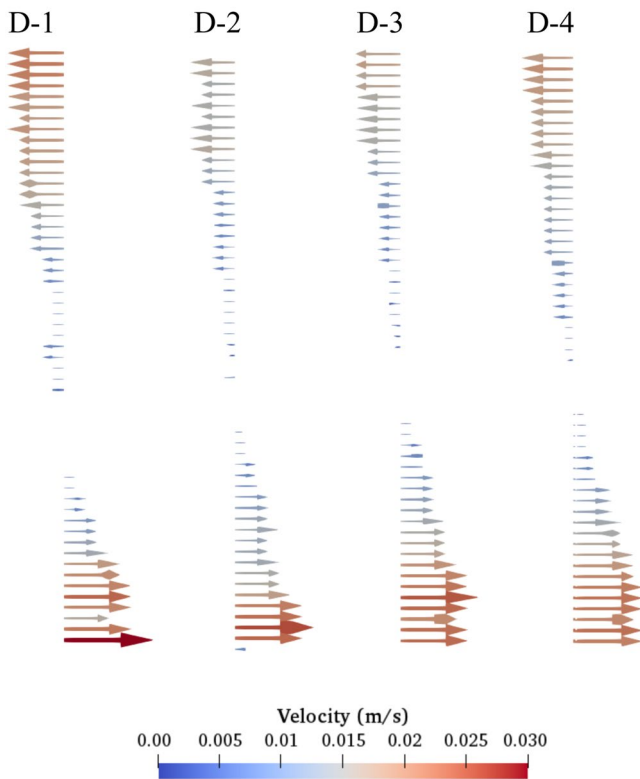
Oa8

Figure 7. The sensitivity of the flow pattern $(u_x(T_\infty), u_z(T_\infty))$ to the length of the averaging period T (Section 3.1). The flow patterns are consistent across different scenarios of $(D-1)$ $t = 0 \to 120$ s $(T = 120$ s$)$; $(D-2)$ $t = 200 \to 320$ s $(T = 120$ s$)$; $(D-3)$ $t = 0 \to 400$ s $(T = 400$ s$)$; and $(D-4)$ $t = 0 \to 620$s $(T = 620$ s$)$. The center of the rotation is found closer to the bed.

below the measured values of δ_i^+ and δ_b^+. Thus the Equation 3 is effective in predicting the potential thickness of the logarithmic layer under ice coverage.

3.4. The Applicability of Quartic Profiles for Ice-Covered Flows

Overall, the entire profiles in almost all ice holes follow closely the quartic solution as shown in Figure 11 and Table 5 following the fitting procedure as discussed in Section 2.5. Surprisingly, the quartic solution works well even in the shallow parts of banks (e.g., Id_2 and Id_7 in Figure 11). In certain locations (Ia_5 and Id_2), the existence of the maximum velocity u_{max} is evident. However, it is not straightforward to assign a unique value of u_{max} in the time-averaged velocity profile for other cases. Here, the optimization of R^2 (see Section 2.5) is useful in justifying the value of η_{max}. As shown in Table 5, the u_{max} location does not typically coincides to the symmetry plane ($\eta = 1$). Rather, the value of η_{max} is frequently greater than 1 and indicates that the maximum velocity appears closer to the ice layer. The asymmetry of the velocity profile is also evident as the value of $\lambda = \frac{u_i^\star}{u_b^\star}$ is mostly less than 1 as shown in Table 5. Therefore, our data supports for a general use of the quartic form for ice-covered flow profiles in rivers. The value of Root Mean Square Error (RMSE) and Absolute Error (AE) are computed to determine the discrepancy between the quartic solution and the observation at each vertical (see Figure 11). Results show that the error is approximately 5% of u_{max} as shown in Figure 12.

3.5. The Structures of Secondary Flow

Under open-surface condition, our results show the signature of a classical circulation in the bridge cross-section under high discharge (Oa and Ob) as shown in Figure 13a (upper panel). On Oa, the secondary flow contains a large vortex occupying the entire thalweg area from the river bed to the free surface. In Ob, the secondary vortex is closer to the bed. This circulation rotates in the clockwise direction (Oa_{4-12} and Ob_{4-12}). In Oa, the center of this circulation locates near the vertical Oa_6 to Oa_9. In Ob, the circulation locates at the vertical Ob_6. In other words, the location of the circulation center is sensitive to the change in flow discharge. In addition to the main circulation, the presence of the outer bank cell is also evident in both Oa and Ob.
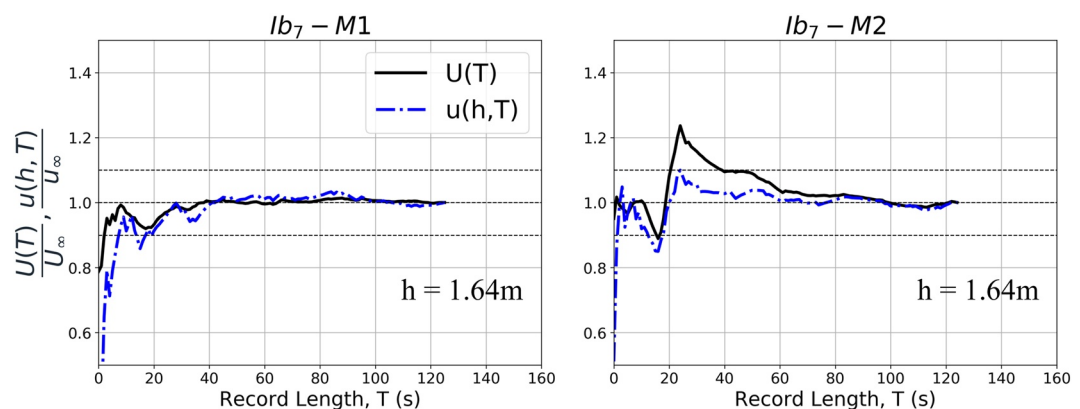

Figure 8. Statistical properties of the depth-averaged velocity $U(T)$ and the time-averaged velocity $u(h, T)$ under ice-covered condition as the function of the record length $T(s)$. Two measurements ($M1$ and $M2$) of same station Ib_7 are shown at the depth $h = 1.64$ m. Here the sample length T is varied from 1 s to the entire record ($T_\infty = 120$ s). The long-term values of $U(T_\infty)$ and $u(h, T_\infty)$ are denoted as U_∞ and $u_\infty(h)$, respectively.
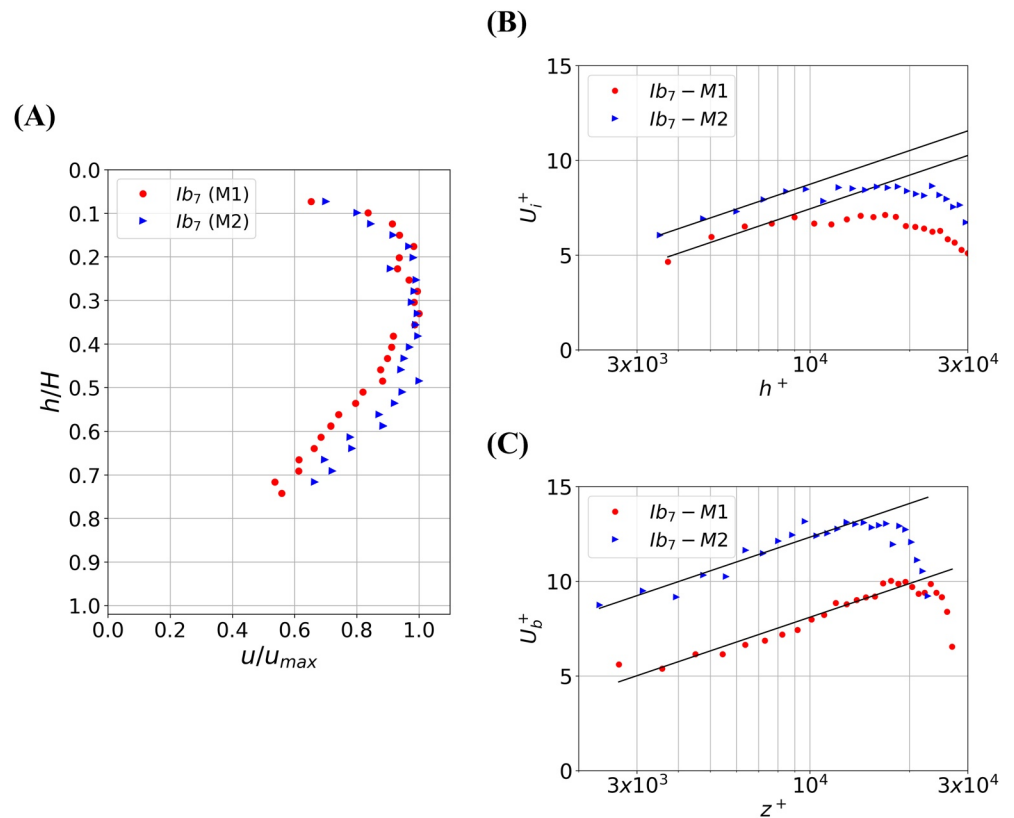
Figure 9. The presence of the logarithmic profile (solid lines) for two consecutive measurements under ice-covered flows. (a) Non-dimensional time-averaged velocity profiles of the first and the second measurement at vertical Ib_7. (b) on the ice layer at the vertical Ib_7; and (c) on the bed layer. The logarithmic law (Equation 6) is written in wall units (see Equations 1 and 2). The separation from the logarithmic law determines the value of the logarithmic layer thickness δ_i^+ and δ_b^+.

Under lower discharges in Oc, Od, and Oe, the secondary flow structure completely changes. The main circulation (clockwise) becomes weaker in the thalweg (Oc_6, Od_{7-8}, and Oe_3). The main circulation moves toward the center of the thalweg as the discharge decreases (Oc, Od, and Oe—see Table 1) as shown in Figure 13 (lower panel). There exist two additional (counter-clockwise) circulations near the outer and inner banks. The extensions of these circulations are significantly large as shown in Oc_{1-4}, Oc_{7-8}, Od_{1-5}, and Od_{9-11}. Three circulations are visible in both Oc and Od and roughly the same size. In brief, the migration of the main circulation is significant as the water level reduces due to the presence of the outer and inner-bank cells.

Our data indicates a significant impact of the ice cover on the secondary flow pattern. Since the cross-section Ia, Ib, Ic, and Id are parallel and separated from each other, it is possible to infer the three-dimensional flow structure at the study site as shown in Figure 14. Under ice coverage, both the main circulation and the flow convergence pattern are altered. Weak circulations are found in the cross-section Ia (Ia_2, and Ia_4). Here there are signatures of two "double-stacked" cells. However, the senses of rotation are in the opposite directions. The existence of such structures cannot be found in Ib. There are two main structures in Ib, the main circulation and the inner bank cell. Both of them rotates in the counter-clockwise direction between $Ib_1–Ib_5$ and $Ib_6–Ib_7$. The secondary flow pattern returns to the regular pattern with a clockwise circulation in the thalweg in Ic and Id. In addition, the inner bank circulation also reverses its direction to the clockwise direction ($Ic_6–Ic_7$ and $Id_6–Id_8$). Therefore, the secondary flow pattern varies drastically from one cross-section to another in the ice-covered bend.

3.6. Shear Velocity Distribution in the Bend

Under open-surface condition, the bed shear velocity $\left(u_b^\star\right)$ is derived using the logarithmic method as summarized in the Table 2. At high discharge (Oa and Ob), $u_b^\star$ can be as high as 0.04 m/s. Despite a slight difference in the value of Q_{Oa} and Q_{Ob}, the distribution of $u_b^\star$ across the cross-section is consistent. In both measurements (Oa

Table 2
Derivation of the Shear Velocity $u_b^\star$ and the Equivalent Roughness Height (z_0) Using the Logarithmic Fitting (Section 2.4) for the Case Oa, Ob, Oc, Od, and Oe (See Table 1)

Case	ℓ (m)	H (m)	$\frac{\delta_b}{H}$	R^2	$u_b^\star$ (m/s)	z_0 (m)	Re_τ	δ_b^+	δ_{theory}^+
Oa_4	16.15	3.66	0.50	0.99	0.0150	0.061	57,876	28,938	8,681
Oa_5	20.12	4.10	0.50	0.94	0.0136	0.0245	55,883	27,941	8,382
Oa_{10}	34.14	3.83	0.50	0.95	0.0090	0.014	34,453	17,226	5,168
Ob_5	19.51	4.10	0.50	0.91	0.0087	0.0003	35,549	17,774	5,332
Ob_6	22.53	4.20	0.30	0.95	0.0079	1.5×10^{-4}	24,613	7,384	3,692
Ob_7	25.60	4.23	0.20	0.99	0.0095	9.7799	57,067	11,413	8,560
Ob_8	28.65	3.99	0.20	0.99	0.0125	0.0365	12,428	2,485	1,864
Ob_9	31.70	3.82	0.20	0.98	0.0124	0.1006	27,596	5,519	4,139
Oc_2	10.36	3.50	0.50	0.99	0.0069	0.0001	24,147	12,073	1,811
Oc_4	16.15	3.95	0.35	0.99	0.0070	0.0188	32,142	11,249	4,821
Oc_5	19.51	4.06	0.20	0.99	0.00796	0.0195	26,764	5,352	4,015
Oc_6	23.16	3.95	0.50	0.98	0.01557	0.4489	61,531	30,765	9,230
Oc_7	28.35	3.65	0.45	0.97	0.0121	0.4760	46,680	21,006	7,002
Od_3	11.89	3.64	0.50	0.99	0.0122	0.5166	44,313	22,156	3,323
Od_4	14.02	3.88	0.40	0.98	0.0078	0.4182	33,176	13,270	4,976
Od_5	16.15	4.09	0.50	0.96	0.0121	0.5056	49,544	24,772	7,431
Od_6	19.20	4.22	0.40	0.97	0.0107	0.4165	51,227	20,491	7,684
Od_7	22.25	4.10	0.50	0.98	0.0109	0.2300	44,573	22,286	6,686
Od_8	24.38	3.80	0.50	0.96	0.0089	0.0570	33,914	16,957	5,087
Od_9	26.52	3.60	0.50	0.93	0.0096	0.2257	34,722	17,361	5,208
Od_{10}	28.65	3.70	0.45	0.99	0.0131	1.2623	49,931	22,469	7,490
Oe_2	15.85	4.01	0.50	0.94	0.0124	2.0462	49,601	24,800	7,440
Oe_3	18.90	4.03	0.35	0.98	0.0088	1.1045	43,687	15,290	6,595
Oe_4	20.42	4.05	0.45	0.96	0.0110	2.2522	47,432	21,344	7,115
Oe_5	23.47	3.76	0.50	0.94	0.0089	0.6461	33,410	16,705	5,011

Note. The friction Reynolds number Re_τ^b and the thickness of the logarithmic layer δ_b^+ are explained in Equation 1. The theoretical bound for δ_{theory}^+ is computed from Equation 3. Only the stations in the thalweg region ($H \geq 3.5$ m) are listed in this table.

and *Ob*), there exists a strong skewed distribution of the shear velocity toward the outer bank as shown the trend line in Figure 15a. The location of the maximum $u_b^\star$ (Oa_2) does not coincide with the maximum depth-averaged velocity location (Oa_4 and Ob_4) (see also Figure 4). The value of $u_b^\star$ decreases gradually from the outer bank to the thalweg toward the value of 0.01 m/s, but it slightly increases near the inner bank. This trend is not observed under low discharges (*Oc* and *Od*) in Figure 15b, which shows that $u_b^\star$ varies in a small range from 0.005 to 0.015 m/s in the thalweg. In brief, a higher discharge leads to a skew $u_b^\star$ distribution with a large magnitude increase (up to four folds) near the outer bank.

Under ice-covered condition, the value of $u_i^\star$ and $u_b^\star$ are derived from two separate methods: (a) the logarithmic law (Section 2.4); and (b) the quartic profile (Section 2.5). Shear velocities from the logarithmic law are listed in Table 4 for all cross-sections *Ia*, *Ib*, *Ic*, and *Id*, while estimates from the quartic solution are shown in Table 5. On both the ice and the bed layers, the quartic solution can provide the value of $u_i^\star$ and $u_b^\star$ in the majority of ice holes as seen in Figure 16. On the contrary, the logarithmic method (solid diamonds) can provide only at certain locations due to the stringent constraints (see Section 2.4) as seen in Table 3. For both $u_i^\star$ and $u_b^\star$, the logarithmic method yields a significantly higher value in comparison to the quartic solution as indicated in Figure 16. Both the logarithmic and the quartic methods indicate that $u_i^\star$ and $u_b^\star$ are elevated near banks. In particular, $u_b^\star$
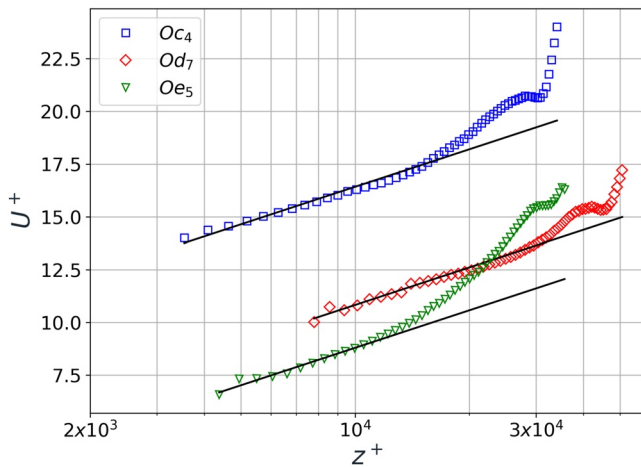
Figure 10. The presence of the logarithmic law (solid lines) at three vertical locations Oc_4 (blue circle), Od_7 (green triangle), Oe_5 (red diamond) under open-surface condition (see Table 1). The logarithmic law (Equation 6) is written in wall units (see Equation 1). The separation from the logarithmic law determines the value of the logarithmic layer thickness δ_b^+. The logarithmic layer is considered as a collection of measured points near the river bed so that the value fitting of $R^2 \geq 0.9$ (see Section 2.4).

can increase from 0.01 m/s (thalweg) to approximately 0.05 m/s near the inner bank. Therefore, shear velocity magnitude varies greatly across the cross-section under ice coverage.

4. Discussion

Ice coverage is an essential component of river hydraulics (Ettema, 2002; Smith & Ettema, 1995; J. Wang et al., 2008). The impacts of ice on flow dynamics in rivers has recently drawn significant attention (Lauzon et al., 2019) from a wide range of viewpoint such as hydrological (Beltaos & Prowse, 2009), morphological (Chassiot et al., 2020; Kämäri et al., 2015), ecological (Knoll et al., 2019) applications. Under the impact of climate change, global coverage of river ice has declined sharply (Peng et al., n.d; Yang et al., 2020) potentially leading to a large-scale transformation of river dynamics in cold regions, especially during spring when snow and ice thaw (Lotsari et al., 2020). Changes in river ice dynamics might lead to new morphological evolution of river deltas in cold regions (Lauzon et al., 2019) as it is known that ice coverage alters sediment transport regime (Lau & Krishnappan, 1985; Turcotte et al., 2011). However, field measurement of ice-covered flows is challenging and thus there are limited data on flow profiles to date (Biron et al., 2019; Ghareh Aghaji Zare et al., 2016; Lotsari et al., 2017). Therefore, this work is intended to revisit this important problem using a modern approach of turbulent flows.

4.1. The Logarithmic Layer Under Open-Surface Condition

Our data support the existence of a universal logarithmic layer (Marusic et al., 2013) for the current site. In particular, our results in Table 2 show that the logarithmic layer is applicable for vertical locations with sufficient depth ($H \geq 3.5$ m) in the thalweg. In these locations, the logarithmic layer is easily detectable as it accounts for a significant portion of the depth (up to 1.5 m as shown in Figure 6). As demonstrated in Figure 10, stations Oc_4, Od_7, and Oe_5 all follow closely the logarithmic profile. It has been known that the logarithmic law might be valid for the majority portions of the flow depth (Biron et al., 1998) in laboratory conditions. The value of δ_b is suggested to be 10%–20% of the total depth (Biron et al., 1998, 2004) under field conditions. Our results show that the logarithmic layer can extend up to half of the total flow depth ($\delta_b/H = 50\%$) regardless of the flow rate. This observation can be seen in the thalweg region and/or near the both banks due to its sensitivity to the local morphological details. As suggested in (Afzalimehr & Rennie, 2009), extension of the logarithmic law can be even beyond the value of 50% with a different channel bed condition (gravel).

Table 3
Derivation of the Shear Velocity $u_b^\star$ and the Equivalent Roughness Height (z_0) Using the Logarithmic Fitting (Section 2.4) for the Case Ia, Ib, Ic, and Id (See Table 1)

Case	ℓ (m)	H (m)	$\frac{\delta_b}{H}$	R^2	$u_b^\star$ (m/s)	z_0 (m)	Re_τ	δ_b^+	δ_{theory}^+
Ia_6	33.83	1.93	0.40	0.9734	0.0161	1.8574	31,088	13,990	4,663
Ib_2	13.53	3.11	0.50	0.9158	0.0128	0.1205	40,001	16,000	6,000
Ib_6	31.82	2.60	0.35	0.9418	0.0137	0.1364	35,623	8,905	5,343
Ib_7	36.39	2.33	0.50	0.9478	0.0477	5.6604	111,125	38,893	16,669
Ic_2	14.63	3.50	0.50	0.9162	0.0102	0.0538	29,113	14,556	4,367
Id_2	12.04	3.43	0.50	0.9620	0.0170	0.998	47,217	23,608	7,083
Id_6	30.33	3.42	0.50	0.9206	0.0089	0.0247	24,773	12,386	3,716
Id_8	39.47	1.65	0.45	0.9921	0.0203	1.5292	26,143	11,764	3,921

Note. The friction Reynolds number Re_τ and the thickness of the logarithmic layer δ_b^+ are explained in Equation 1. The theoretical bound for δ_{theory}^+ is computed from Equation 3.

Table 4
Derivation of the Shear Velocity $u_i^{\star}$ and the Equivalent Roughness Height (z_0) Using the Logarithmic Fitting (Section 2.4) for the Case Ia, Ib, Ic, and Id (See Table 1)

Case	ℓ (m)	H (m)	$\frac{\delta_i}{H}$	R^2	$u_i^{\star}$ (m/s)	z_0 (m)	Re_{τ}	δ_i^+	δ_{theory}^+
Ia_1	8.84	1.72	0.30	0.9033	0.0213	2.0291	29,706	8,912	4,455
Ia_4	23.77	3.46	0.20	0.9499	0.0117	0.0767	33,374	6,675	5,006
Ia_5	28.35	3.39	0.30	0.9276	0.0197	0.7907	27,459	8,238	4,118
Ib_4	22.68	4.01	0.20	0.9174	0.0083	0.0007	27,177	5,435	4,076
Ib_5	27.25	3.68	0.30	0.9837	0.0078	0.0023	23,455	7,037	3,518
Ib_7	36.39	2.33	0.20	0.9921	0.0255	0.4402	48,465	9,693	7,269
Ic_1	10.06	3.04	0.25	0.9262	0.0120	0.4061	30,021	7,505	4,503
Ic_3	19.20	3.74	0.20	0.9398	0.0066	0.0001	21,242	4,248	3,186
Ic_5	28.35	3.48	0.35	0.9630	0.0053	0.0001	15,101	5,285	2,265
Id_2	12.04	3.43	0.25	0.9852	0.0089	0.0117	24,838	6,209	3,725
Id_3	16.61	3.57	0.20	0.9404	0.0041	1×10^{-7}	11,917	2,383	1,787
Id_5	25.76	3.74	0.30	0.9716	0.0053	1×10^{-5}	15,978	4,793	2,396
Id_6	30.33	3.42	0.25	0.9663	0.0070	0.0011	19,543	4,886	2,931
Id_8	39.47	1.65	0.30	0.9845	0.0049	0.0001	6,591	1,977	988
Ie_2	9.14	2.54	0.30	0.9860	0.0101	0.0392	20,941	6,282	3,141
Ie_5	22.86	4.41	0.40	0.9322	0.0044	0.0001	15,930	6,372	2,389
Ie_7	32.00	3.04	0.20	0.9539	0.0034	4.5×10^{-5}	8,313	1,662	1,246

Note. The friction Reynolds number Re_{τ}^i and the thickness of the logarithmic layer δ_i^+ are explained in Equation 1. The theoretical bound for δ_{theory}^+ is computed from Equation 3.

A closer examination of the logarithmic layer thickness in wall units shows that it follows closely the theoretical bounds in Equation 3. Our results in Table 2 and Figure 10 show that the upper bound is applicable for the current site. In fact, the logarithmic layer can extend well beyond the $0.15Re_{\tau}$ limit in many cases as shown in Table 2. Note that the value of $u_b^{\star}$ (and thus Re_{τ}) can be estimated using the Equation 16 from the depth-averaged velocity U. Therefore, our data suggests that the Equation 3 can serve as an estimation for the logarithmic layer thickness if the velocity profile $u(z)$ is not available.

It is known that complex flow fields in shallow areas or rapidly changing bathymetry (Biron et al., 1998; Stone & Hotchkiss, 2007) can lead to the deviation from the logarithmic law (Biron et al., 2004) due to the presence of secondary flows (Petrie & Diplas, 2016). In the presence of complex bathymetry with an adverse pressure gradient, the equilibrium layer could become very thin or completely vanish. Thus the logarithmic law might not exist in certain locations (Bagherimiyab & Lemmin, 2013; Biron et al., 1998). In meandering rivers, secondary flows (Petrie et al., 2013) might impact the distribution of the vertical velocity profile. The absence of the logarithmic layer is also shown to coincide with a strong presence of secondary flow circulation at our site (Oa_6, Oa_7, and Oa_8—see Figure 13a). In particular, the secondary flow is significantly strong in Oa and Ob for locations near both the outer and inner banks. The impact of secondary flow from both banks on the vertical profile is demonstrated in Figure 6. While the variation of the vertical profile in the first 1.5 m depth is minimal in Oa_5, there is a significant deviation of the profile from the logarithmic law near the surface of Oc_6 (Figure 6b), which is a common signature of secondary flows. This behavior is consistent with field observation of (Chauvet et al., 2014), which indicates that the degree of deviation depends on the distance to banks. Thus our results show that it is challenging to perform the logarithmic fitting near both banks even under open-surface condition when the flow depth is limited.

4.2. The Challenge of Using Logarithmic Fitting for Ice-Covered Flows

It is striking that the theoretical bound for δ_i^+ and δ_b^+ (Equation 3) is highly effective. As shown in Tables 3 and 4, the limit of δ_{theory}^+ is satisfied in all available cases for both the ice and river bed layers. This highlights a potential use of the Equation 3 in examining the presence of the logarithmic layers in ice-covered flows. As the value of $u_b^{\star}$

Table 5
Derivation of the Shear Velocity on the Ice Layer $(u_i^\star)$ and the Bed Layer $(u_b^\star)$ Using the Quartic Solution (Section 3.4) for the Case Ia, Ib, Ic, and Id (See Table 1)

Case	ℓ (m)	H (m)	u_{max} (m/s)	R^2	$u_b^\star$ (m/s)	$u_i^\star$ (m/s)	λ	η_{max}
Ia_2	14.33	3.14	0.1451	0.9184	0.0012	0.0016	1.3234	0.7269
Ia_5	28.35	3.39	0.1357	0.9273	0.0073	0.0032	0.4422	1.6729
Ib_2	13.53	3.11	0.1998	0.9916	0.0078	0.0062	0.7886	1.2331
Ib_4	22.68	4.01	0.2115	0.9748	0.0074	0.0048	0.6428	1.4153
Ib_5	27.25	3.70	0.1747	0.9846	0.0074	0.0049	0.6564	1.3977
Ib_6	31.82	2.60	0.1599	0.9795	0.0023	0.0030	1.3067	0.7387
Ib_7	36.39	2.33	0.2036	0.9828	0.0293	0.0193	0.6596	1.3937
Ic_2	14.63	3.50	0.1926	0.9746	0.0071	0.0034	0.4825	1.6223
Ic_4	23.77	3.95	0.1917	0.9765	0.0045	0.0034	0.7535	1.2756
Ic_5	28.35	3.48	0.1844	0.9383	0.0064	0.0050	0.7784	1.2454
Id_2	12.04	3.43	0.1846	0.9119	0.0143	0.0097	0.6777	1.3706
Id_3	16.61	3.57	0.1983	0.9560	0.0075	0.0033	0.4372	1.6791
Id_4	21.18	3.95	0.2023	0.9733	0.0060	0.0023	0.3879	1.7384
Id_5	25.76	3.74	0.1934	0.9812	0.0057	0.0035	0.6142	1.4521
Id_6	30.33	3.42	0.1843	0.9295	0.0084	0.0066	0.7912	1.2300
Id_7	34.90	2.84	0.1707	0.9254	0.0103	0.0046	0.4453	1.6690
Id_8	39.47	1.65	0.1476	0.9380	0.0121	0.0076	0.6305	1.4310
Ie_1	4.57	0.65	0.0839	0.9486	0.0022	0.0020	0.9009	1.1040
Ie_2	9.14	2.54	0.1551	0.9631	0.0088	0.0064	0.7290	1.3059
Ie_3	13.72	3.78	0.1741	0.9781	0.0056	0.0033	0.5836	1.4919
Ie_4	18.29	4.46	0.1596	0.9485	0.0044	0.0021	0.4776	1.6285
Ie_7	32.00	3.04	0.1094	0.9560	0.0063	0.0035	0.5624	1.5194

Note. The local Reynolds number based on shear velocity $u_b^\star$ and water viscosity ν is Re_τ (see Equation 1). The location (η_{max}) and the maximum velocity (u_{max}) are determined by the iterative procedure in Section 3.4.

can be estimated from the quartic method (Section 3.4), the value of δ_{theory}^+ can be deduced from the Equation 3. Therefore, the physical value of δ_{theory} can be recovered. This estimated value of δ_{theory} can guide field measurement in capturing sufficient data in the area of interest.

As the logarithmic fitting is the standard method for estimating $u_b^\star$ in straight channel in open-surface condition (Petrie & Diplas, 2016), it is not clear how to estimate $u_b^\star$ under ice coverage (Attar & Li, 2012; Ghareh Aghaji Zare et al., 2016; A. Sukhodolov et al., 1999), especially in river bends (A. N. Sukhodolov, 2012). Previous works (Ghareh Aghaji Zare et al., 2016; A. Sukhodolov et al., 1999) have assumed the double log-law and used the logarithmic fitting for ice coverage to derive $u_b^\star$. Our results in Tables 3 and 4 indicate that only few vertical stations are qualified to perform logarithmic fitting using our data. The strict requirement of the logarithmic fitting thus does not allow the recovery of $u_b^\star$ value for ice-covered condition in all ice holes. The reason for this challenge might be the presence of the secondary flows as shown in Figure 14. Under ice-covered condition, the magnitude of the secondary flow is approximately 0.1 m/s, which is in the same order as the streamwise component. Field measurements (Demers et al., 2011; A. N. Sukhodolov, 2012; A. Sukhodolov et al., 1999) have shown that complex three-dimensional flow might arise in river bend with ice-covered condition. This complex flow field (Biron et al., 1998, 2004) might deviate the near-wall profiles from the classical logarithmic law. Therefore, it is critical to find a robust method to estimate the value of $u_b^\star$ under field condition.

4.3. The Performance of Quartic Solution

It has been recognized (Biron et al., 1998) in early measurements that the logarithmic method requires sufficient data in the boundary layer. This requirement is typically not satisfied in field measurements (Attar & Li, 2012)
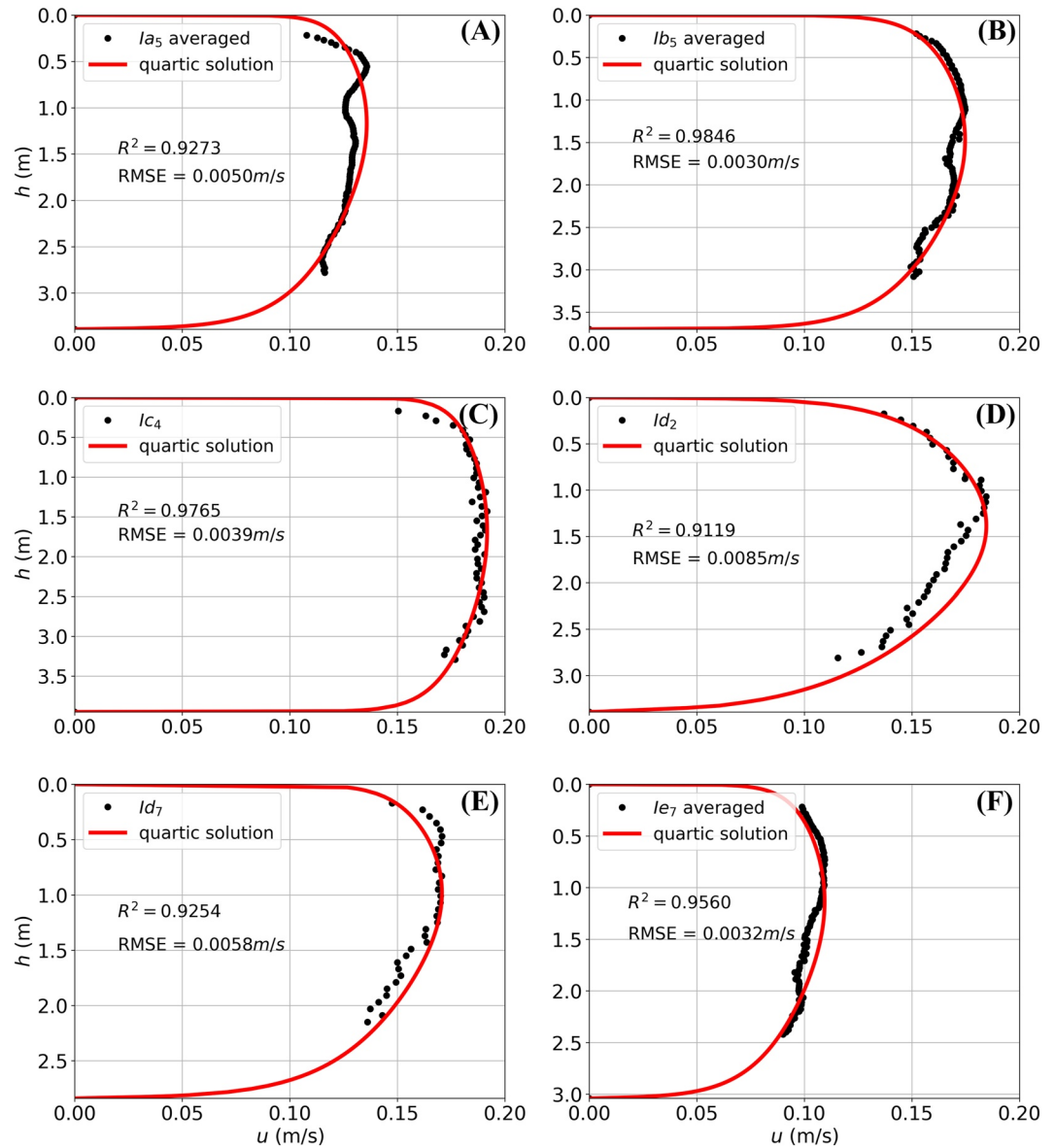
Figure 11. The agreement between the measured profiles and the quartic solution. The fitting procedure provides the shear velocity on the river bed $\left(u_b^\star\right)$ and the ice layer $\left(u_i^\star\right)$ in Section 2.5. The details of the available data are described in Table 5 for all ice holes. The averaged profile (from two measurements $M1$ and $M2$) is used for the cross-sections Ia, Ib, and Ie. The discrepancies between the model and the observations are computed with RMSE.

as it is challenging to obtain measured data near the river bed and the ice layer. Our data in Figure 11 shows that the quartic solution agrees well with field measurement. As it uses the entire velocity profile, the quartic solution can be applied in the majority of ice holes. Note that the quartic solution is designed (Guo et al., 2017) so that it coincides to the logarithmic layer in the limit of $z^+ \to 0$. This feature relaxes the strict requirement of Section 2.4. Therefore, the quartic solution can provide an estimation for the shear velocity $u_b^\star$ even if there are limited measurements along the vertical profile.

One important assumption of the quartic solution is the separation of flows in the ice and the bed layer by a distinct maximum velocity location $u_{\max}(z_{\max})$. As shown in Figure 1, the velocity profile is governed by different sets of shear velocities (Ghareh Aghaji Zare et al., 2016; Guo et al., 2017; A. Sukhodolov et al., 1999). The presence of $u_{\max}$ in the analytical solution is apparent because the shear stress distribution along the depth is assumed to be linear (Guo et al., 2017). However, it is not clear whether or not a distinct $u_{\max}$ is evident in field

Table 6
The Accuracy of the Logarithmic Fitting

Case	H (m)	$u_{lo}^{\star}$ (m/s)	$u^{\star}$ (m/s)	$u_{up}^{\star}$ (m/s)	z_0^{lo} (m)	z_0 (m)	z_0^{up} (m)
Oc_2 (bed)	3.50	0.0065	0.0069	0.0073	4.28×10^{-5}	0.0001	0.0003
Ob_5 (bed)	4.10	0.0079	0.0087	0.0095	0.0002	0.0003	0.0004
Ib_7 (bed)	2.33	0.0401	0.0477	0.0553	4.0442	5.6604	7.2766
Id_6 (bed)	3.42	0.0076	0.0089	0.0102	0.0044	0.0247	0.0450
Id_8 (bed)	1.65	0.0192	0.0203	0.0214	0.2415	1.5292	2.8169
Ia_1 (ice)	1.72	0.0116	0.0213	0.0310	0.6902	2.0291	3.3680
Ib_5 (ice)	3.68	0.0072	0.0078	0.0084	0.0008	0.0023	0.0038
Ib_7 (ice)	2.33	0.0213	0.0255	0.0297	0.2339	0.4402	0.6465
Ic_5 (ice)	3.48	0.0048	0.0053	0.0059	2.5×10^{-5}	0.0001	0.0002
Id_8 (ice)	1.65	0.0040	0.0049	0.0058	3×10^{-6}	0.0001	0.0002

Note. The lower and upper limits of $u^{\star}$ and z_0 for the ice and bed layers in representative verticals according to 95% confidence level.

measurements. Our results show that it is challenging to determine the location z_{max} from our field data since the time-averaged profile does not typically show a distinct u_{max}. While our fitting procedure attains good agreement ($R^2 \geq 0.9$) with measurement data, the determination of u_{max} location does affect the overall shape of the profile. The maximum velocity location η_{max} is the critical factor to attain a high value of R^2. In fact, the value of u_{max} and its position in near-bank locations are usually determined decisively as shown in Figure 11 (Id_2). However, the minimal variation of the velocity profile $u(z)$ in the mixing core region prevents a straightforward approach to locate η_{max} (Ic_4) in the thalweg. Therefore, an iterative procedure as shown in Section 3.4 is necessary to obtain the maximum value for R^2. The difficulty of locating a single value for η_{max} also highlights the limitation of the quartic method. It is required that the velocity profile has a distinct maximum value, which is not guaranteed in the presence of complex bathymetry. The strong secondary flow as illustrated in Figure 14 near Ia_5, Ic_4, and Id_7 might deviate the vertical velocity profiles from the quartic form.

Figure 12. Error analysis of profile fitting using the quartic solution for Ia_5, Ib_5, Ic_4, Id_2, Id_7, and Ie_7. The observed values (u_{obs}) are plotted against the fitted results ($u_{quartic}$). The line of perfect agreement is shown in black. The linear regression line is displayed by a blue dashed line, which shows a good agreement between the observed and fitted data. The maximum absolute errors are shown indicating the upper and lower bound errors of 0.014(m/s).

4.4. Secondary Flow Patterns

It has been long known that flows in streams and rivers have helical patterns (Demers et al., 2011) which possess secondary flow (SF) components. In contrast to the randomness of turbulent structures, secondary flows appear in time-averaged velocity profiles (Zhong et al., 2016) as separate entities. Secondary flows originate from two main sources: channel curvature (Prandtl's first kind); and heterogeneous turbulent stresses (Prandtl's second kind) (Nikora & Roy, 2012). In the first kind, secondary flow is directed from the inner bank toward the outer bank as the flow approaches a bend (Kang et al., 2011). The impacts of curvature on the formation of the main flow cell are clear and were discussed in many studies (Koken et al., 2013; Van Balen et al., 2010). The second kind of secondary flow is formed in response to roughness heterogeneity (Rodríguez & García, 2008). In this flow type, the fluctuations of turbulent shear stress are sustained across the cross-section, leading to the formation of many flow cells (Nezu et al., 1993) occupying the entire cross-section (Blanckaert et al., 2010). The distribution of shear stresses along the cross-sectional perimeter (e.g., bed, bank, and surface) determines the types and number of flow cells, and how these cells interact with each other (Albayrak & Lemmin, 2011; Blanckaert et al., 2010; Nikora et al., 2019; Rodríguez & García, 2008). While this phenomenon has been postulated for natural channels (Nezu et al., 1993), its existence has rarely been investigated under field condition (Chauvet et al., 2014).
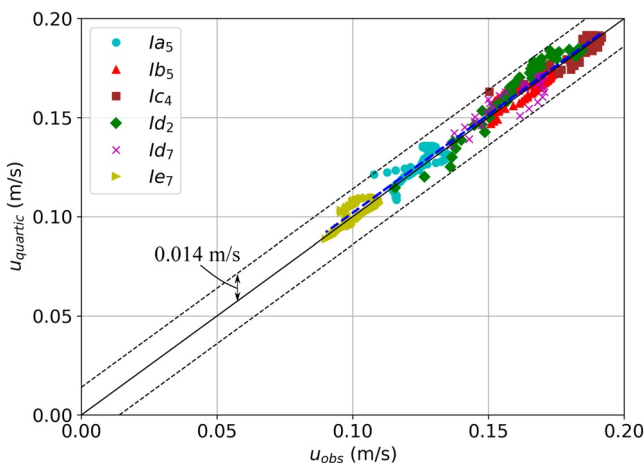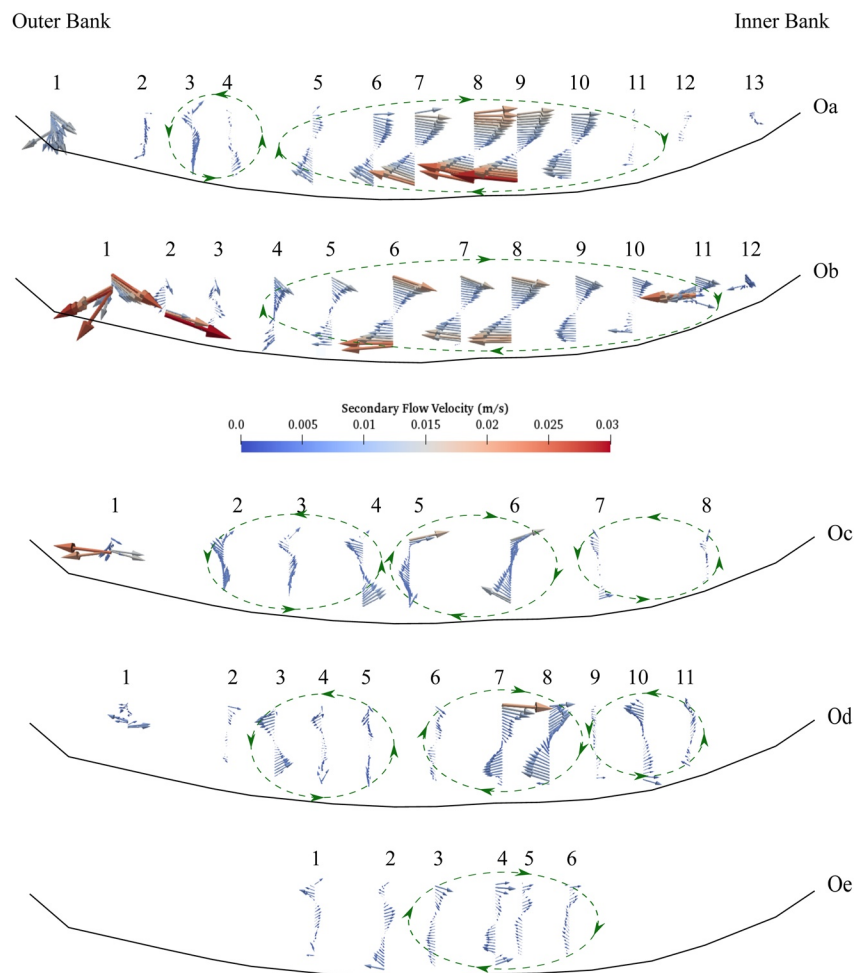
Figure 13. The dependence of secondary flow structures at the bridge cross-section on flow discharge (See Table 1) under open-surface condition. The secondary flow vectors are visualized with the Rozovskii method. The vertical location of each ADCP measurement on the cross-section is marked with numbers. Number of vectors are reduced by a factor of two for visibility purpose.

Under open-surface condition, our results in Figure 13 show a striking dependence of secondary flow patterns on the flow discharge. The dominance of the main circulation in *Oa* and *Ob* is replaced by the co-existence of multiple-cell structures in *Oc*, *Od*, and *Oe*. In effect, our results show a transition from a single circulation (high discharge) to multiple circulations (low discharge). This transition is important because it highlights the potential linkage between the flow discharge with the strength of the main circulation. Our results in *Oa* suggest that the impact of channel curvature, which induces the main circulation, is dominant when the flow discharge is sufficiently large. At low discharges, this dominance is lost. The main circulation and the bank cells all play important roles in creating the helical patterns across the cross-section. This phenomenon agrees with the field observation of (Chauvet et al., 2014) and laboratory data of (Albayrak & Lemmin, 2011). Future works might be needed in understanding the precise threshold at which this transition occurs.

Comparing our results in Figures 13 and 14, it is evident that the ice cover adds further complexities in the secondary flow patterns. The maximum velocity is found to be $u_{max} \approx 0.19$ m/s in the thalweg area (see Figure 11). Meanwhile, the corresponding secondary flow velocity in the same vertical (Ic_2) remains below 0.015 m/s, which is less than 10% of u_{max}. This range of secondary flow agrees with other observations in literature (Tsai & Ettema, 1994a). While the flow convergence pattern is still visible at *Ia*, the secondary flow patterns at other cross-sections vary greatly in a short distance of approximately 20 m. These results indicate that the large-scale flow structure of the entire reach has been modified with the presence of the ice cover. There is no apparent existence of a large-scale circulation at *Ia*, *Ib*, and *Ic* as shown in Figure 14. A circulation reemerges at *Id* near the
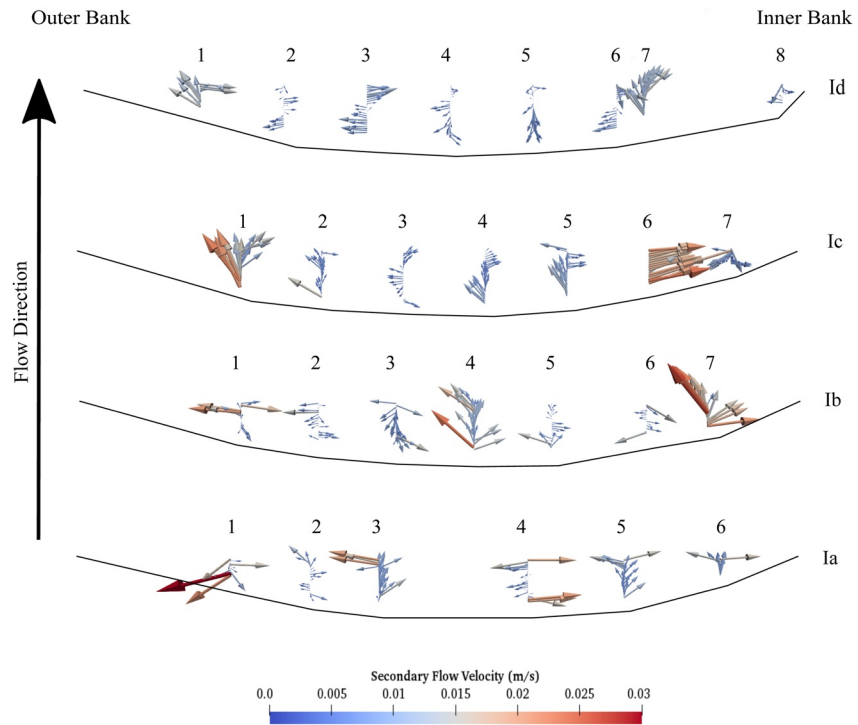
Figure 14. The spatial variability of secondary flow structures across four consecutive cross-sections under ice-covered condition in February 2021. The cross-sections *Ia*, *Ib*, *Ic*, and *Id* are parallel to each other and separated by a distance of 6.1 m as shown in Figure 13. The flow direction is from *Ia* to *Id* in the South-North direction (bottom to top). The ice holes are numbered from the outer bank to the inner bank as shown in Table 1. Number of vectors are reduced by a factor of two for visibility purpose.

outer bank but it is also accompanied by a change in the flow convergence pattern. The intermittent appearance of the circulation suggests that the large-scale circulation is truly a local phenomenon, which could depend on the bathymetry and the flow depth.

Laboratory experiment (Urroz & Ettema, 1994a) suggests that the secondary flow under ice-covered condition could have a special structure (double-stacked) where two sets of vortices are found on top of each other in the thalweg. Field measurements of (Demers et al., 2011) suggest that the double-stacked vortices might exist at the bend entrance. However, our results in Figure 14 do not support the persistent existence of such a structure in this case in all cross-section *Ia*, *Ib*, *Ic*, and *Id*. Our result only shows a single vortex in *Id* close to the outer bank. It has been shown (Lotsari et al., 2017) that flow depth can alter the secondary flow pattern of ice-covered flows at river bends by changing the direction of the high-velocity core (Attar & Li, 2013). Therefore, the disagreement from our measurements with the laboratory experiment of (Urroz & Ettema, 1994a) might be explained by the difference in aspect ratio between field and laboratory scales. In the experimental setup of (Urroz & Ettema, 1994a), the range of aspect ratio (AR) is $10 < AR < 20$ (large aspect ratio). In our case, the aspect ratio is estimated to be approximately 10. Thus the double-stacked vortices might appear only at certain aspect ratios of river cross-sections.

4.5. Shear Stress Distribution

In the literature, the period of ice coverage is assumed to be a quiescent period of sediment transport (Ettema, 2002) since the value of $u_b^\star$ is assumed to be smaller than the open-surface counterpart. Comparing the Figures 16b and 15b under similar flow discharges, it is evident that the ice coverage contributes to a significant increase of $u_b^\star$ near banks. The value of $u_b^\star$ can reach from 0.02 to 0.05 m/s in the vicinity of the inner and outer banks under ice-covered condition. Such a magnitude is comparable to the bed shear stress under open-surface condition near the outer bank as shown in Figure 15 at a much higher level of flow discharge (*Oa*). This finding is rather surprising since the ice-covered flow discharge is much smaller in comparison to the open-surface ones as shown
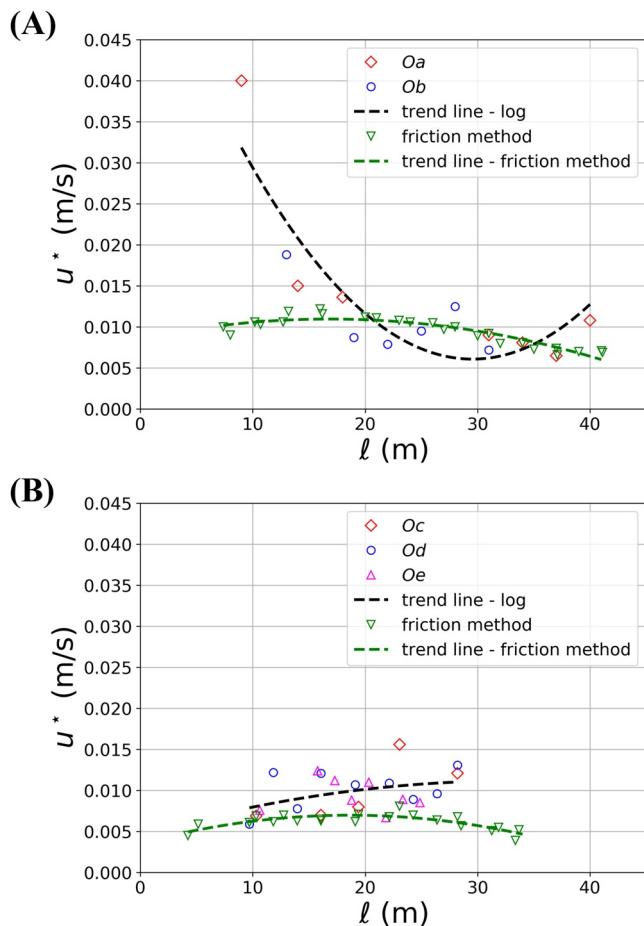
(A)

(B)

Figure 15. Shear velocity $\left(u_b^\star\right)$ profiles on the river bed under open-surface condition. The value of $u_b^\star$ is derived by the logarithmic fitting method in Section 2.4. The relative location ℓ to the outer bank (along the East direction) is chosen to represent the vertical locations (see Figure 4). Two levels of flow discharge are examined (a) high discharge (Q_{Oa} = 23.41 m³/s and Q_{Ob} = 23.87 m³/s); and (b) low discharge (Q_{Oc} = 14.3 m³/s, Q_{Od} = 12.2 m³/s, and Q_{Oe} = 6.82 m³/s). The details of the flow measurements are reported in Table 1.

in Table 1. Such a sharp increase indicates a potential impact on sediment transport processes in shallow areas. Future efforts should be carried out to investigate this phenomenon further.

Overall, the friction method (2.6) provides an excellent estimation of $u_b^\star$ with minimal input information, especially at low discharge. Under low flow condition (*Oc* and *Od*) in Figure 15b, the friction method predicts that $u_b^\star \approx 0.007$ m/s where as the logarithmic method suggests that $u_b^\star \approx 0.01$ m/s. However, the it cannot provide an accurate estimation of $u_b^\star$ at high discharge (*Oa* and *Ob*) as shown in Figure 15a. The friction method gives a reasonable estimation of $u_b^\star \approx 0.01$ m/s throughout the cross-section. However, it cannot capture the extreme values of $u_b^\star$ near the outer bank. A careful approach must be carried out to examine shear velocities near banks separately.

4.6. Limitation

In laboratory measurement or numerical simulation (Ma et al., 2021), turbulent statistics can be obtained by extending the averaging time T to an extremely large value (e.g., $T = 50\frac{H}{u_b^\star}$). Under field conditions, it is challenging to obtain reliable data for the velocity profile (Biron et al., 1998) in large rivers. It is because of a well-known limitation of the ADCP signal near the river bed. It requires a long period of measurement (Petrie & Diplas, 2016) to provide an accurate time-averaged velocity profile. Therefore, the duration of measurement (Buffin-Bélanger & Roy, 2005) plays an important role in attaining statistically convergent results. Under open-surface condition, our time series length is set to be a minimum of 600 s in all vertical locations. Note that the T_∞ = 10 min has been reported to be sufficient for ADCP measurement (Chauvet et al., 2014) to reconstruct secondary flow features at field scale.

Since the field campaign can be only carried out when the ice cover is sufficiently thick ($\geq$0.25 m) for this Red River, it thus requires that the air temperature in the field campaign should be sufficiently low (a typical situation in February). The ADCP M9 sensor can function properly in the range of air temperature ($>-20°C$). However, a prolonged campaign in few hours in many ice holes leads to the deterioration of the signal quality as the sensor surface can become frozen easily and make a long acquisition infeasible. In contrast to the open-surface condition, the record length (T_∞) of our ice measurements is relatively short (2 min) to prevent the *M*9 sensor surface from freezing. Such a short duration (2 min) might not be enough to obtain the fully convergent profile $u_\infty(z)$ ($\pm$5%) (Marian et al., 2021). In addition, it is not possible to obtain boundary layer flow in the first distance of 0.25 m from the ice layer due to the configuration of ADCP measurement. Future works need to rely on other modalities such as Acoustic Doppler Velocimetry (ADV) to capture this boundary layer flow more accurately in conjunction with ADCP data. In addition, the comparison between ADV and ADCP data can provide sufficient data for uncertainty analysis (Longo et al., 2012) to determine precisely the required sampling duration T_∞ for ice-covered flows.

In laboratory condition (Flack & Schultz, 2010) or numerical simulation (Ma et al., 2021), the value of the equivalent roughness height, z_0, can be related to the physical roughness (Flack & Schultz, 2010). However, it has been shown (Petrie & Diplas, 2016) that the value of z_0 cannot be determined reliably using field measurement data (Petrie et al., 2013). Under open-surface condition, the obtained values of z_0 can vary from 1.0×10^{-4} m to the order of 10.0 m. This variability agrees with other field studies in literature (Petrie & Diplas, 2016; Petrie et al., 2013). In particular, this range of obtained z_0 does not agree with the measured sediment grain size at the site, which has $d_{50} \approx 0.5$ mm (Galloway & Nustad, 2012). In ice-covered case, our estimation for z_0 varies from 1.0×10^{-7} to 2.03 m as shown in Table 4 for ice roughness. This estimation does not agree with the physical
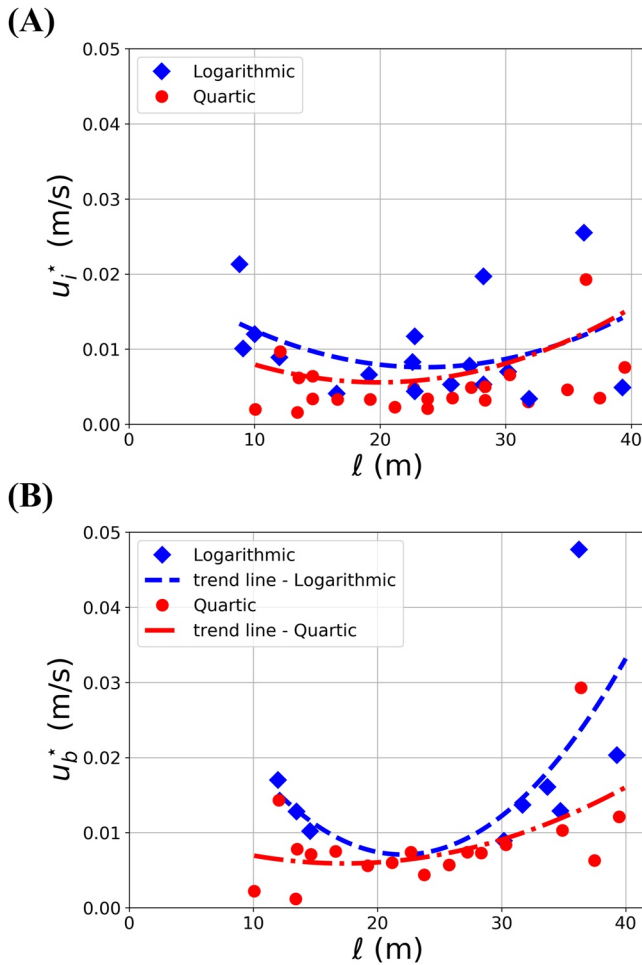
(A)

(B)

Figure 16. The distribution of shear velocity on: (a) the ice layer $\left(u_i^\star\right)$, and (b) the river bed $\left(u_b^\star\right)$ across the bend apex cross-section. The blue diamonds represent the shear velocities which are derived from the logarithmic methodology (Section 2.4). The red circles represent the shear velocities, which are derived from the quartic methodology. The dash-dotted lines show the trend lines of $u_i^\star$ and $u_b^\star$ with each type of fitting methodology.

range of ice roughness (Bushuk et al., 2019), which is at the limit of 0.02 m. Therefore the fitted value of z_0 cannot be interpreted as the actual physical roughness.

5. Conclusion

The impacts of ice coverage on velocity profiles in a river bend are investigated using Acoustic Doppler Current Profiler. The main goal is to evaluate the changes in the vertical velocity profiles as well as the secondary flow pattern as the ice coverage emerges in a river bend. In addition, the quartic method is examined as an alternative procedure to derive the bed shear velocity instead of using the classical logarithmic method. Our results show that the vertical flow profiles and the bed shear velocity are altered significantly under ice coverage. The following conclusions are made:

1. Our data support the existence of a universal logarithmic layer close to the river bed (within 20% of the local depth) in the thalweg of the bend under open-surface condition. In certain locations, the logarithmic layer can extend up to 50% of the total depth. In wall units, the theoretical bound (Equation 3) is well respected.
2. Under ice-covered condition, the logarithmic law is not recognized for the majority of the vertical locations. In the cases where it is applicable, the logarithmic layer is restricted in 20% of the total depth.
3. It might be challenging to use the logarithmic law to derive the shear velocities $u_b^\star$ and $u_i^\star$ due to the lack of data both temporally and spatially near the bed and the ice layers. On the other hand, the quartic solution (Guo et al., 2017) is helpful in determining these shear velocities. The quartic solution, however, is sensitive to the determination of z_{max}, which might result in an underestimation of the shear stresses.
4. Our results show that the ice coverage changes the spatial distribution of the bed shear stress across the cross-section. Under the open-surface condition, the spatial distribution of bed shear velocity is skewed toward the outer bank, especially under a high discharge. Under the ice-covered condition, high values of bed shear velocity appear on both banks. The elevated values of shear stresses near the banks suggest that sediment transport processes might be active during winter in shallow areas.
5. Under open-surface condition, the secondary flow pattern is dependent on the flow discharge. At high discharge, a single circulation dominates the overall pattern. At low discharge, two counter-rotating circulations, which have reverse senses of rotation to the high discharge one, mutually exist. Under ice-covered condition, the secondary flow pattern becomes highly complex. Multiple circulations are found simultaneously with alternating senses of rotation. This feature is distinctively different from the open-surface counterparts.

Conflict of Interest

The authors declare no conflicts of interest relevant to this study.

Data Availability Statement

LiDAR Data from the State Water Commission of North Dakota (https://lidar.dwr.nd.gov/) were used in the creation of this manuscript. The hydrological data is extracted from the measurement data of the United States Geological Survey (USGS) station (USGS FARGO 09020104). Figures were made with Matplotlib version 3.2.1 (Caswell et al., 2020), available under the Matplotlib license at https://matplotlib.org/. Velocity

contours and vectors were created through the open-source Paraview software (5.4.1). The flow velocity data was first processed using the Velocity Mapping Toolbox (VMT) version (4.09) licensed, available at https://hydroacoustics.usgs.gov/movingboat/VMT/VMT.shtml. The raw data is processed with our MATLAB (v. 9.6) scripts. Our raw data is available at https://github.com/trunglendsu/ESIP/tree/main/ADCP_Data.

References

Afzalimehr, H., & Rennie, C. (2009). Determination of bed shear stress using boundary layer parameters in a gravel-bed river. *Hydrological Sciences Journal*, *54*(1), 147–159. https://doi.org/10.1623/hysj.54.1.147

Albayrak, I., & Lemmin, U. (2011). Secondary currents and corresponding surface velocity patterns in a turbulent open-channel flow over a rough bed. *Journal of Hydraulic Engineering*, *137*(11), 1318–1334. https://doi.org/10.1061/(asce)hy.1943-7900.0000438

Anwar, H. O. (1986). Turbulent structure in a river bend. *Journal of Hydraulic Engineering*, *112*(8), 657–669. https://doi.org/10.1061/(asce)0733-9429(1986)112:8(657)

Attar, S., & Li, S. (2012). Data-fitted velocity profiles for ice-covered rivers. *Canadian Journal of Civil Engineering*, *39*(3), 334–338. https://doi.org/10.1139/l2012-001

Attar, S., & Li, S. (2013). Momentum, energy and drag coefficients for ice-covered rivers. *River Research and Applications*, *29*(10), 1267–1276. https://doi.org/10.1002/rra.2611

Bagherimiyab, F., & Lemmin, U. (2013). Shear velocity estimates in rough-bed open-channel flow. *Earth Surface Processes and Landforms*, *38*(14), 1714–1724. https://doi.org/10.1002/esp.3421

Bathurst, J. C., Hey, R. D., & Thorne, C. R. (1979). Secondary flow and shear stress at river bends. *Journal of the Hydraulics Division*, *105*(10), 1277–1295. https://doi.org/10.1061/jyceaj.0005285

Beltaos, S., & Prowse, T. (2009). River-ice hydrology in a shrinking cryosphere. *Hydrological Processes: International Journal*, *23*(1), 122–144. https://doi.org/10.1002/hyp.7165

Biron, P. M., Buffin-Bélanger, T., & Martel, N. (2019). Three-dimensional turbulent structures at a medium-sized confluence with and without an ice cover. *Earth Surface Processes and Landforms*, *44*(15), 3042–3056. https://doi.org/10.1002/esp.4718

Biron, P. M., Lane, S. N., Roy, A. G., Bradbrook, K. F., & Richards, K. S. (1998). Sensitivity of bed shear stress estimated from vertical velocity profiles: The problem of sampling resolution. *Earth Surface Processes and Landforms: The Journal of the British Geomorphological Group*, *23*(2), 133–139. https://doi.org/10.1002/(sici)1096-9837(199802)23:2<133::aid-esp824>3.0.co;2-n

Biron, P. M., Robson, C., Lapointe, M. F., & Gaskin, S. J. (2004). Comparing different methods of bed shear stress estimates in simple and complex flow fields. *Earth Surface Processes and Landforms: The Journal of the British Geomorphological Research Group*, *29*(11), 1403–1415. https://doi.org/10.1002/esp.1111

Blanchard, R. A., Ellison, C. A., Galloway, J. M., & Evans, D. A. (2011). *Sediment concentrations, loads, and particle-size distributions in the red river of the north and selected tributaries near Fargo, North Dakota, during the 2010 spring high-flow event (Technical Report)*. U. S. Geological Survey.

Blanckaert, K., Duarte, A., & Schleiss, A. J. (2010). Influence of shallowness, bank inclination and bank roughness on the variability of flow patterns and boundary shear stress due to secondary currents in straight open-channels. *Advances in Water Resources*, *33*(9), 1062–1074. https://doi.org/10.1016/j.advwatres.2010.06.012

Buffin-Bélanger, T., & Roy, A. G. (2005). 1 min in the life of a river: Selecting the optimal record length for the measurement of turbulence in fluvial boundary layers. *Geomorphology*, *68*(1–2), 77–94. https://doi.org/10.1016/j.geomorph.2004.09.032

Bushuk, M., Holland, D. M., Stanton, T. P., Stern, A., & Gray, C. (2019). Ice scallops: A laboratory investigation of the ice–water interface. *Journal of Fluid Mechanics*, *873*, 942–976. https://doi.org/10.1017/jfm.2019.398

Caswell, T. A., Droettboom, M., Lee, A., Hunter, J., Firing, E., Sales De Andrade, E., et al. (2020). matplotlib/matplotlib: REL: v3. 3.1. Zenodo.

Chassiot, L., Lajeunesse, P., & Bernier, J.-F. (2020). Riverbank erosion in cold environments: Review and outlook. *Earth-Science Reviews*, *207*, 103231. https://doi.org/10.1016/j.earscirev.2020.103231

Chaudhry, M. H. (2007). *Open-channel flow*. Springer Science & Business Media.

Chauvet, H., Devauchelle, O., Métivier, F., Lajeunesse, E., & Limare, A. (2014). Recirculation cells in a wide channel. *Physics of Fluids*, *26*(1), 016604. https://doi.org/10.1063/1.4862442

Chen, G., Gu, S., Li, B., Zhou, M., & Huai, W. (2018). Physically based coefficient for streamflow estimation in ice-covered channels. *Journal of Hydrology*, *563*, 470–479. https://doi.org/10.1016/j.jhydrol.2018.06.032

Demers, S., Buffin-Bélanger, T., & Roy, A. (2011). Helical cell motions in a small ice-covered meander river reach. *River Research and Applications*, *27*(9), 1118–1125. https://doi.org/10.1002/rra.1451

Engel, F. L., & Rhoads, B. L. (2016). Three-dimensional flow structure and patterns of bed shear stress in an evolving compound meander bend. *Earth Surface Processes and Landforms*, *41*(9), 1211–1226. https://doi.org/10.1002/esp.3895

Ettema, R. (2002). Review of alluvial-channel responses to river ice. *Journal of Cold Regions Engineering*, *16*(4), 191–217. https://doi.org/10.1061/(asce)0887-381x(2002)16:4(191)

Flack, K. A., & Schultz, M. P. (2010). Review of hydraulic roughness scales in the fully rough regime. *Journal of Fluids Engineering*, *132*(4). https://doi.org/10.1115/1.4001492

Galloway, J. M., & Nustad, R. A. (2012). *Sediment loads in the red river of the north and selected tributaries near Fargo, North Dakota, 2010—2011 (Technical Report)*. US Geological Survey.

Gao, W., Cheng, W., & Samtaney, R. (2020). Large-eddy simulations of turbulent flow in a channel with streamwise periodic constrictions. *Journal of Fluid Mechanics*, *900*, A43. https://doi.org/10.1017/jfm.2020.512

Ghareh Aghaji Zare, S., Moore, S. A., Rennie, C. D., Seidou, O., Ahmari, H., & Malenchak, J. (2016). Estimation of composite hydraulic resistance in ice-covered alluvial streams. *Water Resources Research*, *52*(2), 1306–1327. https://doi.org/10.1002/2015wr018096

Guo, J., Shan, H., Xu, H., Bai, Y., & Zhang, J. (2017). Exact solution for asymmetric turbulent channel flow with applications in ice-covered rivers. *Journal of Hydraulic Engineering*, *143*(10), 04017041. https://doi.org/10.1061/(asce)hy.1943-7900.0001360

Hanjalić, K., & Launder, B. (1972). Fully developed asymmetric flow in a plane channel. *Journal of Fluid Mechanics*, *51*(2), 301–335. https://doi.org/10.1017/s0022112072001211

Hurther, D., & Lemmin, U. (2000). Shear stress statistics and wall similarity analysis in turbulent boundary layers using a high-resolution 3-D ADVP. *IEEE Journal of Oceanic Engineering*, *25*(4), 446–457. https://doi.org/10.1109/48.895352

Kämäri, M., Alho, P., Veijalainen, N., Aaltonen, J., Huokuna, M., & Lotsari, E. (2015). River ice cover influence on sediment transportation at present and under projected hydroclimatic conditions. *Hydrological Processes*, *29*(22), 4738–4755. https://doi.org/10.1002/hyp.10522

Kang, S., Lightbody, A., Hill, C., & Sotiropoulos, F. (2011). High-resolution numerical simulation of turbulence in natural waterways. *Advances in Water Resources*, *34*(1), 98–113. https://doi.org/10.1016/j.advwatres.2010.09.018

Knoll, L. B., Sharma, S., Denfeld, B. A., Flaim, G., Hori, Y., Magnuson, J. J., et al. (2019). Consequences of lake and river ice loss on cultural ecosystem services. *Limnology and Oceanography Letters*, *4*(5), 119–131. https://doi.org/10.1002/lol2.10116

Koken, M., Constantinescu, G., & Blanckaert, K. (2013). Hydrodynamic processes, sediment erosion mechanisms, and Reynolds-number-induced scale effects in an open channel bend of strong curvature with flat bathymetry. *Journal of Geophysical Research: Earth Surface*, *118*(4), 2308–2324. https://doi.org/10.1002/2013jf002760

Lane, S. N., Bradbrook, K., Richards, K., Biron, P., & Roy, A. (2000). Secondary circulation cells in river channel confluences: Measurement artefacts or coherent flow structures? *Hydrological Processes*, *14*(11–12), 2047–2071. https://doi.org/10.1002/1099-1085(20000815/30)14:11/12<2047::aid-hyp54>3.0.co;2-4

Lau, Y. L., & Krishnappan, B. G. (1985). Sediment transport under ice cover. *Journal of Hydraulic Engineering*, *111*(6), 934–950. https://doi.org/10.1061/(asce)0733-9429(1985)111:6(934)

Lauzon, R., Piliouras, A., & Rowland, J. C. (2019). Ice and permafrost effects on delta morphology and channel dynamics. *Geophysical Research Letters*, *46*(12), 6574–6582. https://doi.org/10.1029/2019gl082792

Longo, S., Liang, D., Chiapponi, L., & Jiménez, L. A. (2012). Turbulent flow structure in experimental laboratory wind-generated gravity waves. *Coastal Engineering*, *64*, 1–15. https://doi.org/10.1016/j.coastaleng.2012.02.006

López, F., & García, M. H. (1999). Wall similarity in turbulent open-channel flow. *Journal of Engineering Mechanics*, *125*(7), 789–796. https://doi.org/10.1061/(asce)0733-9399(1999)125:7(789)

Lotsari, E., Dietze, M., Kämäri, M., Alho, P., & Kasvi, E. (2020). Macro-turbulent flow and its impacts on sediment transport potential of a subarctic river during ice-covered and open-channel conditions. *Water*, *12*(7), 1874. https://doi.org/10.3390/w12071874

Lotsari, E., Kasvi, E., Kämäri, M., & Alho, P. (2017). The effects of ice cover on flow characteristics in a subarctic meandering river. *Earth Surface Processes and Landforms*, *42*(8), 1195–1212. https://doi.org/10.1002/esp.4089

Ma, R., Alamé, K., & Mahesh, K. (2021). Direct numerical simulation of turbulent channel flow over random rough surfaces. *Journal of Fluid Mechanics*, *908*, A40. https://doi.org/10.1017/jfm.2020.874

Marian, M., Kim, J., & Kim, D. (2021). Impact of the sampling duration on the uncertainty of averaged velocity measurements with acoustic instruments. *Hydrological Processes*, *35*(4), e14125. https://doi.org/10.1002/hyp.14125

Marusic, I., Monty, J. P., Hultmark, M., & Smits, A. J. (2013). On the logarithmic region in wall turbulence. *Journal of Fluid Mechanics*, *716*. https://doi.org/10.1017/jfm.2012.511

Moradi, G., Vermeulen, B., Rennie, C. D., Cardot, R., & Lane, S. N. (2019). Evaluation of ADCP processing options for secondary flow identification at river junctions. *Earth Surface Processes and Landforms*, *44*(14), 2903–2921. https://doi.org/10.1002/esp.4719

Muste, M., Yu, K., Pratt, T., & Abraham, D. (2004). Practical aspects of ADCP data use for quantification of mean river flow characteristics; part II: Fixed-vessel measurements. *Flow Measurement and Instrumentation*, *15*(1), 17–28. https://doi.org/10.1016/j.flowmeasinst.2003.09.002

Muste, M., Yu, K., & Spasojevic, M. (2004). Practical aspects of adcp data use for quantification of mean river flow characteristics; Part I: Moving-vessel measurements. *Flow Measurement and Instrumentation*, *15*(1), 1–16. https://doi.org/10.1016/j.flowmeasinst.2003.09.001

Nezu, I., Tominaga, A., & Nakagawa, H. (1993). Field measurements of secondary currents in straight rivers. *Journal of Hydraulic Engineering*, *119*(5), 598–614. https://doi.org/10.1061/(asce)0733-9429(1993)119:5(598)

Nikora, V., & Roy, A. G. (2012). Secondary flows in rivers: Theoretical framework, recent advances, and current challenges. Gravel bed rivers: Processes, tools, environments (pp. 3–22).

Nikora, V., Stoesser, T., Cameron, S. M., Stewart, M., Papadopoulos, K., Ouro, P., et al. (2019). Friction factor decomposition for rough-wall flows: Theoretical background and application to open-channel flows. *Journal of Fluid Mechanics*, *872*, 626–664. https://doi.org/10.1017/jfm.2019.344

Parker, G. (1991). Selective sorting and abrasion of river gravel. II: Applications. *Journal of Hydraulic Engineering*, *117*(2), 150–171. https://doi.org/10.1061/(asce)0733-9429(1991)117:2(150)

Parthasarathy, R., & Muste, M. (1994). Velocity measurements in asymmetric turbulent channel flows. *Journal of Hydraulic Engineering*, *120*(9), 1000–1020. https://doi.org/10.1061/(asce)0733-9429(1994)120:9(1000)

Peng, X., Zhang, T., Frauenfeld, O. W., Du, R., Jin, H., & Mu, C. (n.d.). A holistic assessment of 1979–2016 global cryospheric extent. *Earth's Future*, *9*(8), e2020EF001969

Petrie, J., & Diplas, P. (2016). Evaluation of the logarithmic law of the wall for river flows. *River Research and Applications*, *32*(5), 1082–1093. https://doi.org/10.1002/rra.2920

Petrie, J., Diplas, P., Gutierrez, M., & Nam, S. (2013). Data evaluation for acoustic Doppler current profiler measurements obtained at fixed locations in a natural river. *Water Resources Research*, *49*(2), 1003–1016. https://doi.org/10.1002/wrcr.20112

Prowse, T. D. (2001a). River-ice ecology. i: Hydrologic, geomorphic, and water-quality aspects. *Journal of Cold Regions Engineering*, *15*(1), 1–16. https://doi.org/10.1061/(asce)0887-381x(2001)15:1

Prowse, T. D. (2001b). River-ice ecology. ii: Biological aspects. *Journal of Cold Regions Engineering*, *15*(1), 17–33. https://doi.org/10.1061/(asce)0887-381x(2001)15:1(17)

Rodríguez, J. F., & García, M. H. (2008). Laboratory measurements of 3-D flow patterns and turbulence in straight open channel with rough bed. *Journal of Hydraulic Research*, *46*(4), 454–465. https://doi.org/10.3826/jhr.2008.2994

Shen, C., & Lemmin, U. (1997). A two-dimensional acoustic sediment flux profiler. *Measurement Science and Technology*, *8*(8), 880–884. https://doi.org/10.1088/0957-0233/8/8/008

Smith, B. T., & Ettema, R. (1995). *Ice-cover influence on flow and bedload transport in dune-bed channels*. Iowa Institute of Hydraulic Research, the University of Iowa.

Soulsby, R. (1981). Measurements of the Reynolds stress components close to a marine sand bank. *Marine Geology*, *42*(1–4), 35–47. https://doi.org/10.1016/0025-3227(81)90157-2

Stoesser, T., Ruether, N., & Olsen, N. R. B. (2010). Calculation of primary and secondary flow and boundary shear stresses in a meandering channel. *Advances in Water Resources*, *33*(2), 158–170. https://doi.org/10.1016/j.advwatres.2009.11.001

Stone, M. C., & Hotchkiss, R. H. (2007). Evaluating velocity measurement techniques in shallow streams. *Journal of Hydraulic Research*, *45*(6), 752–762. https://doi.org/10.1080/00221686.2007.9521813

Sukhodolov, A., Thiele, M., Bungartz, H., & Engelhardt, C. (1999). Turbulence structure in an ice-covered, sand-bed river. *Water Resources Research*, *35*(3), 889–894. https://doi.org/10.1029/1998wr900081

Sukhodolov, A. N. (2012). Structure of turbulent flow in a meander bend of a lowland river. *Water Resources Research*, *48*(1). https://doi.org/10.1029/2011wr010765

Tatinclaux, J.-C., & Gogus, M. (1983). Asymmetric plane flow with application to ice jams. *Journal of Hydraulic Engineering*, *109*(11), 1540–1554. https://doi.org/10.1061/(asce)0733-9429(1983)109:11(1540)

Thellman, A., Jankowski, K. J., Hayden, B., Yang, X., Dolan, W., Smits, A. P., & O'Sullivan, A. M. (2021). The ecology of river ice. *Journal of Geophysical Research: Biogeosciences*, *126*(9), e2021JG006275. https://doi.org/10.1029/2021jg006275

Tsai, W.-F., & Ettema, R. (1994a). Ice cover influence on transverse bed slopes in a curved alluvial channel. *Journal of Hydraulic Research*, *32*(4), 561–581. https://doi.org/10.1080/00221686.1994.9728355

Tsai, W.-F., & Ettema, R. (1994b). Modified eddy viscosity model in fully developed asymmetric channel flows. *Journal of Engineering Mechanics*, *120*(4), 720–732. https://doi.org/10.1061/(asce)0733-9399(1994)120:4(720)

Turcotte, B., Morse, B., Bergeron, N. E., & Roy, A. G. (2011). Sediment transport in ice-affected rivers. *Journal of Hydrology*, *409*(1–2), 561–577. https://doi.org/10.1016/j.jhydrol.2011.08.009

Urroz, G. E., & Ettema, R. (1994a). Application of two-layer hypothesis to fully developed flow in ice-covered curved channels. *Canadian Journal of Civil Engineering*, *21*(1), 101–110. https://doi.org/10.1139/l94-010

Urroz, G. E., & Ettema, R. (1994b). Small-scale experiments on ice-jam initiation in a curved channel. *Canadian Journal of Civil Engineering*, *21*(5), 719–727. https://doi.org/10.1139/l94-077

Van Balen, W., Blanckaert, K., & Uijttewaal, W. S. (2010). Analysis of the role of turbulence in curved open-channel flow at different water depths by means of experiments, les and rans. *Journal of Turbulence*, *11*, N12. https://doi.org/10.1080/14685241003789404

Volino, R. J., & Schultz, M. P. (2018). Determination of wall shear stress from mean velocity and Reynolds shear stress profiles. *Physical Review Fluids*, *3*(3), 034606. https://doi.org/10.1103/physrevfluids.3.034606

Wang, F., Huai, W., Liu, M., & Fu, X. (2020). Modeling depth-averaged streamwise velocity in straight trapezoidal compound channels with ice cover. *Journal of Hydrology*, *585*, 124336. https://doi.org/10.1016/j.jhydrol.2019.124336

Wang, J., Sui, J.-y., & Karney, B. W. (2008). Incipient motion of non-cohesive sediment under ice cover—An experimental study. *Journal of Hydrodynamics*, *20*(1), 117–124. https://doi.org/10.1016/s1001-6058(08)60036-0

Weiss, A., Clark, S. P., Rennie, C. D., Moore, S. A., & Ahmari, H. (2015). Estimation of total suspended solids concentration from adcp backscatter and hydraulic measurements. *Journal of Hydraulic Research*, *53*(5), 670–677. https://doi.org/10.1080/00221686.2015.1076531

Whiting, P. J., & Dietrich, W. E. (1990). Boundary shear stress and roughness over mobile alluvial beds. *Journal of Hydraulic Engineering*, *116*(12), 1495–1511. https://doi.org/10.1061/(asce)0733-9429(1990)116:12(1495)

Wilcock, P. R. (1996). Estimating local bed shear stress from velocity observations. *Water Resources Research*, *32*(11), 3361–3366. https://doi.org/10.1029/96wr02277

Yang, X., Pavelsky, T. M., & Allen, G. H. (2020). The past and future of global river ice. *Nature*, *577*(7788), 69–73. https://doi.org/10.1038/s41586-019-1848-1

Zhong, Q., Chen, Q., Wang, H., Li, D., & Wang, X. (2016). Statistical analysis of turbulent super-streamwise vortices based on observations of streaky structures near the free surface in the smooth open channel flow. *Water Resources Research*, *52*(5), 3563–3578. https://doi.org/10.1002/2015wr017728